



HAL
open science

Mean wind flow reconstruction of a high-rise building based on variational data assimilation using sparse pressure measurements

Mohamed Yacine Ben Ali, Gilles Tissot, Sylvain Aguinaga, Dominique Heitz,
Etienne Mémin

► To cite this version:

Mohamed Yacine Ben Ali, Gilles Tissot, Sylvain Aguinaga, Dominique Heitz, Etienne Mémin. Mean wind flow reconstruction of a high-rise building based on variational data assimilation using sparse pressure measurements. *Journal of Wind Engineering and Industrial Aerodynamics*, 2022, 231 (105204), pp.16/105204. 10.1016/j.jweia.2022.105204 . hal-03602618

HAL Id: hal-03602618

<https://hal.science/hal-03602618>

Submitted on 9 Mar 2022

HAL is a multi-disciplinary open access archive for the deposit and dissemination of scientific research documents, whether they are published or not. The documents may come from teaching and research institutions in France or abroad, or from public or private research centers.

L'archive ouverte pluridisciplinaire **HAL**, est destinée au dépôt et à la diffusion de documents scientifiques de niveau recherche, publiés ou non, émanant des établissements d'enseignement et de recherche français ou étrangers, des laboratoires publics ou privés.

Mean wind flow reconstruction of a high-rise building based on variational data assimilation using sparse pressure measurements

M.Y. Ben Ali^{a,b,c,*}, G.Tissot^a, S. Aguinaga^b, D.Heitz^c, E. Mémin^a

^a*Inria/IRMAR, Fluminance team, Campus universitaire de Beaulieu, F-35042 Rennes, France*

^b*Centre Scientifique et Technique du Bâtiment (CSTB), 11 rue Henri Picherit, F-44300 Nantes, France*

^c*INRAE, UR OPAALE, F-35044 Rennes Cedex, France*

Abstract

Data assimilation consists in combining a model and measurements in order to estimate the state of the system. In wind engineering, the interest to take advantage of both sources of information is extremely high. As a matter of fact, on the one hand, measurements in wind tunnel experiments are in practice extremely sparse and, on the other hand, stationary numerical models based on Reynolds averaged Navier-Stokes (RANS) fail to predict the time-averaged wake accurately. Variational data assimilation (VDA) techniques are defined as high-dimensional optimisation problems, the solution of which is determined through an adjoint method. In practical applications, where only wall pressure measurements on the building are available, an accurate mean flow reconstruction is very challenging, especially in regions far away from any measurements. In the present paper, spatially distributed forces are considered as a control parameter on the momentum equation or the turbulence closure equations. These forcings are interpreted as corrections brought to the turbulence closure. Consequently, the problem corresponds to a high-dimensional optimisation problem for a spatially distributed variable with sparse pressure measurements. Some guidelines are brought here to perform accurate and physically consistent reconstructions for wind engineering applications. In order to deal as closely as possible with a practical application, this study focuses on the realizable revision of the $k - \epsilon$ RANS model applied on a high-rise building wake flow. In particular, some regularisation strategies as well as efficient techniques for control parameter selection and identification are provided.

1 Introduction

Because of their potential long-time exposure to strong atmospheric winds, high-rise buildings may exhibit problematic tearing affecting security [1, 2, 3]. To infer how wind flow affects these structures, some authors [4, 3] have used physical models and numerical simulations for a long time. In order to predict accurately the pressure distribution on the building, the surrounding flow field has to be well represented, but the development of computationally affordable models that fits experimental informations in realistic 3D configurations is still today challenging.

Wind tunnel experiments are conducted on reduced-scale models at the design stage, leading to reliable experimental load predictions thanks to years of progress on flow measurement techniques. High-Frequency Pressure Integration (HFPI) [5] is one of the most common techniques employed for wind load prediction. This sparse wall pressure measurement may lead to misinterpretations on the local pressure field when complex geometries are considered. Moreover, although techniques such as Particle Image Velocimetry (PIV) [6] allow in principle to obtain planar or even full 3D data [7] velocity fields, the cost is considerably higher.

More recently, made possible by the substantial progresses in computational fluid dynamics, numerical simulations of atmospheric boundary layer flow over these large structures have been carried out. Both steady simulations embedding turbulence models within the Reynolds averaged Navier–Stokes (RANS) and large eddy simulations (LES) were investigated to give an insight into the time-averaged flow profile. Several studies were conducted to compare their relative performances and assess their applicability to the prediction of flow around buildings. [1, 8, 9, 10, 11, 12, 13]. In most of these studies, flow-field around cubic-buildings were analysed, and deficiencies of the eddy viscosity modelling in the $k - \epsilon$ model [14] were put forward (e.g., by Murakami et al. [1]). These include the stagnation point anomaly [15, 16] with overestimation of turbulent kinetic energy near the frontal corner and the resulting underestimation of the size of separated boundary layers. Another reported anomaly is the underestimation of turbulent kinetic energy in the wake resulting in an overestimation of the size of

*Corresponding author:

Email address: mohamed-yacine.ben-ali@inria.fr (M.Y. Ben Ali)

Preprint submitted to Elsevier

March 9, 2022

34 the recirculation zone. These accuracy issues strongly hinder the predictive
35 abilities of the model to reproduce wall-pressure measurements. Although,
36 LES leads to intrinsically superior performances [11, 12, 17], they are com-
37 putationally expensive. Moreover, they carry some difficulties, such as the
38 definition of time-dependent inlet and wall boundary conditions [18, 19, 20].

39 Measurements and numerical simulations provide complementary pieces
40 of information. The aim of the data-model coupling strategy, which consti-
41 tutes the core of the present work, is to move beyond the respective limita-
42 tions of data and models by taking advantage of all available information.
43 This strategy will allow us to provide an effective solution to address turbu-
44 lence modelling errors at a reasonable cost, informed by data obtained from
45 realistic experimental procedures. The concept of data-model coupling, or
46 more commonly referred to as data-assimilation (DA), comes from estima-
47 tion theory, and was first been applied to numerical weather prediction [21].

48 Two large classes of DA exist. Statistical techniques based on Bayesian
49 inference leads to sequential strategies such as the Kalman filter. It has been
50 used to estimate optimal flow parameters from data affected by a high un-
51 certainty level [22, 23]. It is opposed to variational methods [24, 25], where
52 the estimation problem is written as an optimisation problem. The latter
53 is solved through gradient descent optimization techniques based on the
54 adjoint of the linear tangent dynamics operator or an ensemble approxima-
55 tion of it. These methodologies have been carried out for direct numerical
56 simulations (DNS) or LES models in [26, 27, 28, 22, 29, 30].

57 In this line of thought, formal uncertainty quantification (UQ) tech-
58 niques have been employed to address the modelling errors underlying the
59 closure constants of RANS systems in probabilistic terms [31, 32, 33, 34,
60 35, 36]. In a recent work by Shirzadi et al. [37], global coefficients of the
61 standard $k - \epsilon$ model were adapted for unstable atmospheric boundary layer
62 (ABL) flow around high-rise buildings using Monte-Carlo optimisation tech-
63 niques. More recently, in Ben Ali et al. [38] the global coefficients of the
64 realizable revision of the $k - \epsilon$ model were also calibrated for wind-loads
65 prediction on a high-rise building of ratio $H/D = 4.9$ (same configuration
66 as the present paper). In this latter work, the authors used wind tunnel
67 pressure measurements in a variational data assimilation (VDA) framework.
68 The VDA is then applied for a detailed analysis of the considered turbulence
69 model. Local sensitivity to the global turbulence coefficients is discussed,
70 and a calibration process was conducted to investigate the limitations of
71 the models through hold/relax closure hypothesis scenarios. It was re-

72 ported that the VDA technique is indeed able to provide insights on the
73 model variability through calibration of model closure coefficients. It was
74 observed that variabilities of the solution were strongly constrained and did
75 not allow the flow to reach an effective region of the state space for accurate
76 estimations of both the wind-loads and the recirculation zone, highlighting,
77 in consequence, the rigidity of the standard closure model. To overcome
78 such restrictions, the authors have considered a so-called *weak constraint*
79 by defining an additive forcing term to allow the solution to deviate from
80 the default model. Better flow reconstructions have been obtained, but no
81 detailed studies have been performed to determine the best way to relax the
82 dynamical constraint for flow reconstruction. Many control parameters and
83 formulations of the optimisation problem can be considered. The present
84 study complements the work of Ben Ali et al. [38] to explore in details the
85 possible control parameters choices to estimate at best the flow surrounding
86 the building.

87 In the last few years, studies dealing mainly with fundamental and indus-
88 trial oriented flow configurations, e.g., airfoils, infinite cylinder, backward
89 step, have been considered for data assimilation (DA) flow reconstruction.
90 A hierarchy of procedures has been proposed. In [39, 40], laminar steady
91 Navier–Stokes equations corrected by a direct forcing on the momentum
92 equations have been used to assimilate synthetic particle image velocime-
93 try (PIV) data. For turbulent flows, DA with RANS turbulence models
94 have been explored [41, 42, 43, 44]. Franceschini and Sipp [44] have partly
95 addressed closure errors to the transport equation of eddy-viscosity in the
96 Spalart–Allmaras model [45]. In other works [41, 42, 43], data (either syn-
97 thetic or experimental) were assimilated, and turbulence model errors were
98 addressed in the turbulent energy production as it constitutes one common
99 issue for the prediction of a variety of flow configurations. In these stud-
100 ies, reconstructions of several benchmark flow configurations, ranging from
101 one-dimensional channel flows to 2D airfoil flows, were performed under
102 the framework of both ensemble Kalman [46] and VDA. It should be noted
103 that all these studies were investigated in bi-dimensional flow configura-
104 tions, in which turbulence is often generated at a unique integral scale. To
105 our knowledge, three-dimensional cases of complex flow interactions, such
106 as building-lower atmospheric boundary layer interaction, are still largely
107 unexplored with VDA.

108 Ben Ali et al. [38] focused on exploiting the VDA framework to extract
109 physical information on the flow and identify deficiencies in the turbulence

110 closure modelling of the RANS. In the present study, the objective is to
111 perform the best flow estimation as possible with a distributed control pa-
112 rameter based on a RANS model and on wall-pressure measurements for
113 wind-engineering applications. The main contributions are :

- 114 • Applying the VDA on a realistic wind engineering estimation problem
115 combining wall-pressure measurements with a routinely used indus-
116 trial three-dimensional RANS code;
- 117 • Determining the best choice of distributed control parameter to avoid
118 overfitting and obtain accurate reconstructions;
- 119 • Proposing a Sobolev gradient descent direction and comparing it with
120 penalty techniques to regularise the solution and drastically accelerate
121 the convergence.

122 To these ends, a large set of assimilations with various choices are per-
123 formed and compared to provide guidelines for VDA estimations in wind
124 engineering.

125 This paper is organized as follows. In section 2, the flow configuration
126 is presented. In section 3, the methodology to derive the VDA approach
127 is introduced. A modified set of RANS equations is presented, motiva-
128 tions for the choices of parameter and regularization solution are given.
129 In section 4, the numerical setup is presented. In section 5.1, the data-
130 assimilation results of the various parametrization strategies are shown. Fi-
131 nally, to obtain accurate reconstructions, a modified model that combines
132 previous parametrizations is investigated in section 5.2.

133 2. Flow configuration

134 The present work was conducted on an isolated high-rise building with
135 a square section and an aspect ratio of $H/D \simeq 4.9$ for which $H = 147$ m
136 is the height and $D = 30$ m the width at full scale. Measurements were
137 produced from experiments held in CSTB (Nantes, France) as part of the
138 thesis of Sheng et al. [47]. In his work, two types of experiments were
139 carried out, using the HFPI for wall-pressure and PIV plans for the near
140 wake flow. It should be recall that only the wall-pressure was considered in
141 this work as input data for the data-assimilation procedure. PIV plans from
142 the same experiment were used only for an external validation purpose. For
143 illustration, figure 1 shows the 3D view of the case study from both the
144 experiments and our computational setup.

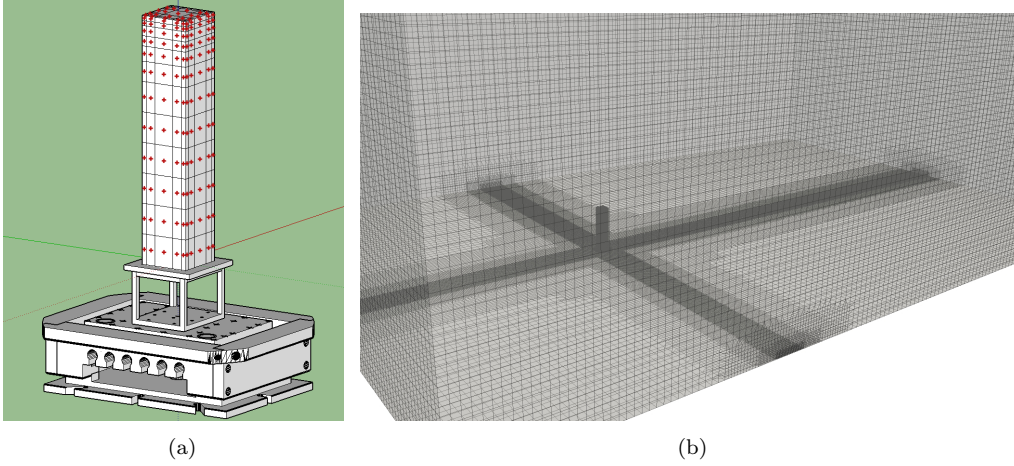


Figure 1: Flow configuration (a) the scaled model of the building with positions of pressure measurements (red dots), (b) the full scale building in the computational domain.

145 3. Methodology

146 This section briefly presents the variational data-assimilation framework,
 147 which was developed in [38].

148 With the variational approach [24, 25], the estimation problem is ex-
 149 pressed in terms of the minimization of an objective functional, which mea-
 150 sures the mismatch between the model predictions and the data, under
 151 the constraint that the optimal state obeys to the model dynamics. In
 152 the context of time-averaged models, the data assimilation problem can be
 153 formulated as

$$\min_{\alpha} \mathcal{J}(\alpha, \mathbf{X}(\alpha), \mathbf{Y}) \quad (1a)$$

$$\text{subject to } M_i(\alpha, \mathbf{X}(\alpha)) = 0 \quad i = 1, \dots, N, \quad (1b)$$

154 where $\mathcal{J}()$ is the objective functional that quantifies the discrepancy
 155 between the assimilated data and the model predictions, with \mathbf{Y} referring
 156 to the measurements and \mathbf{X} to the flow variables. This objective is then
 157 minimized under the constraint of N flow governing equations M_i .

158 3.1. Objective functional

159 Following [38], the objective functional is constructed as follows. First,
 160 the experimental pressure is scaled consistently with the pressure of the

161 model using the pressure coefficient $C_p = \frac{P - P_\infty}{\frac{1}{2}\rho U_{\text{ref}}^2}$, with the reference velocity
 162 U_{ref} (resp. reference pressure P_∞) being the far upstream velocity (resp.
 163 pressure) at $H_{\text{ref}} = \frac{2}{3}H$. The specific functional reads as follows

$$\mathcal{J}(P, \alpha) = \frac{1}{2} \|\rho U_{\text{ref}}^2 \Delta C_p^w\|_{R^{-1}}^2 + \|\nabla \alpha\|_{B^{-1}}^2, \quad (2)$$

164 where $\Delta C_p^w = C_{p_{\text{obs}}}^w - \mathcal{I}(C_p^w)$ with the subscript w standing for wall-pressure
 165 and obs for measurements. The interpolation operator \mathcal{I} maps the wall-
 166 pressure coefficient of the numerical model to the pressure coefficient at the
 167 sensor position. The covariance matrix, R , between measurements allows
 168 to take into account experimental uncertainties and potential correlations
 169 between measurements. The norm $\|\cdot\|_{R^{-1}}$ is induced by the inner product
 170 $(\cdot, \cdot)_{R^{-1}} = (\cdot, R^{-1}\cdot)$, where (\cdot, \cdot) stands for the Euclidean inner product.
 171 Similarly, $\|\cdot\|_{B^{-1}}$ is induced by the weighted $L^2(\Omega)$ inner product $(\cdot, \cdot)_{B^{-1}} =$
 172 $(\cdot, B^{-1}\cdot)_{L^2(\Omega)}$.

173 It can outline here the strongly sparse nature of the partial pressure ob-
 174 servations making the estimation problem difficult. To cope with this diffi-
 175 culty, an L^2 regularization term is added to penalize the gradient magnitude
 176 of the spatially distributed control parameter α . The covariance matrix B
 177 penalises allows to adjust the degree of regularity to be prescribed. A too-
 178 small penalty leads to irregular solutions, while strong penalties deteriorate
 179 reconstruction performances by imposing a too-smooth solution. In our
 180 case, spatial homogeneity for this constraint is assumed, and the confidence
 181 matrix B is considered diagonal and uniform. Its inverse is straightforwardly
 182 expressed as

$$B_{ii}^{-1} = \zeta_i \left(\max \left| \frac{\partial \mathcal{J}^0}{\partial \alpha} \right| \right).$$

183 in which ζ_i is a positive free parameter and subscript i stands for the vector
 184 and matrix component. The other term is a scaling to ensure dimensional
 185 homogeneity.

186 3.2. Constraint definition

187 This section is dedicated to the specification of the dynamical model \mathbf{M} .
 188 The Reynolds averaged Navier-Stokes equations are considered, with the
 189 realizable version of the $k - \epsilon$ turbulence model [48]:

$$\frac{\partial(\rho U_j U_i)}{\partial x_j} + \frac{\partial P}{\partial x_i} - \frac{\partial}{\partial x_j} \left[\mu_{eff} \left(\frac{\partial U_i}{\partial x_j} + \frac{\partial U_j}{\partial x_i} \right) \right] = F_i, \quad (3a)$$

$$\frac{\partial U_j}{\partial x_j} = 0, \quad (3b)$$

$$\frac{\partial \rho U_j k}{\partial x_j} - \frac{\partial}{\partial x_j} \left[\left(\mu + \frac{\mu_t}{\sigma_k} \right) \frac{\partial k}{\partial x_i} \right] - \mu_t \left(\frac{\partial U_i}{\partial x_j} + \frac{\partial U_j}{\partial x_i} \right) \frac{\partial U_i}{\partial x_j} + \rho \epsilon = 0, \quad (3c)$$

$$\frac{\partial \rho U_j \epsilon}{\partial x_j} - \frac{\partial}{\partial x_j} \left[\left(\mu + \frac{\mu_t}{\sigma_\epsilon} \right) \frac{\partial \epsilon}{\partial x_i} \right] - C_1(S, k, \epsilon) S \epsilon + C_2 \frac{\epsilon^2}{k + \sqrt{\mu \epsilon}} = F_\epsilon. \quad (3d)$$

190 where U , ρ and P denote the average velocity, the density and the pres-
 191 sure, respectively. The turbulent kinetic energy and the energy dissipation
 192 density are denoted k and ϵ . Here, $\mu_{eff} = (\mu_t + \mu)$ stands for an effective
 193 viscosity gathering both the molecular and the isotropic eddy viscosity, with

$$\mu_t = C_\mu \rho \frac{k^2}{\epsilon}. \quad (4)$$

194 Details on the closure constants are provided in Appendix A. It is worth
 195 noting that, through the Boussinesq approximation, the isotropic compo-
 196 nent $\frac{2}{3}\rho k$ of the Reynolds stress is absorbed into P . Therefore, in the com-
 197 putation of the pressure coefficient required for the objective functional (2),
 198 the isotropic part must be subtracted to obtain $C_p = \frac{P - P_\infty - \frac{2}{3}\rho k}{1/2\rho U_{ref}^2}$. Note the
 199 addition of two forcing terms \mathbf{F} and F_ϵ , respectively to the RANS equations
 200 and to the turbulence dissipation transport equation. Those forcing terms
 201 constitute the control parameter α as detailed in section 3.3. Recalling
 202 that the corrections brought by the forcing term F_ϵ solely correspond to the
 203 previous work of [38].

204 3.3. Parameter choice

205 In the construction of the Reynolds averaged Navier-Stokes equations,
 206 some assumptions are performed at different levels. The first one pertains
 207 to the Boussinesq hypothesis and consists in modelling the Reynolds stress
 208 tensor in the momentum equation by a diffusive term weighted by a scalar
 209 eddy viscosity. The value of the eddy viscosity is determined by an algebraic
 210 equation involving statistical quantities related to the turbulence. At a sec-
 211 ond level, transport equations of these turbulent quantities are constructed.

212 Some semi-empirical terms acting as sources and sinks in these transport
213 equations allow closing the equations.

214 In the present work, for each layer of assumptions, a possible parametriza-
215 tion is proposed as given in the system (3d). Herein, some detailed motiva-
216 tions are provided for the parameter choice.

217 *Parametrising the momentum equation.* At the first level, one aim to bring
218 a direct correction to the mean deformation field. In theory, the exact
219 modeling of the deformation should properly include the mechanisms of
220 energy transfer between the mean field towards the turbulence scales and
221 vice versa. However, the Boussinesq hypothesis leads to a unidirectional
222 energy transfer. From this point of view, a volume force term added to the
223 mean momentum equations can be proposed as a control parameter enabling
224 us to relax the Boussinesq hypothesis and bring non-diffusive mechanisms.
225 Without a priori knowledge of its form, it is straightforward to consider a
226 vector force

$$\mathbf{F}_1 = \mathbf{f}_u$$

227 which is later-on referred to as a *raw* form. As this raw form lacks of struc-
228 turation, a more refined shape, yet with a simple expression, of this force
229 is also investigated. Here, it is aimed to ensure some consistency between
230 the deformation correction prescribed by this force and the fact that the
231 Reynolds stress induces it. Corrections can be restricted to regions where
232 the turbulence appears to be the most active and where the turbulence
233 model is likely to be prone to strong errors. Shear layers in separated flows
234 are challenging for turbulence models due to strong flow inhomogeneity and
235 anisotropy, which is poorly represented by eddy diffusion models. We con-
236 sider here addressing only corrections due to the flow inhomogeneity, that
237 is, regions with a strong gradient of turbulent kinetic energy. Thus, a sim-
238 ple model of more refined forcing term for the direct deformation correction
239 may be defined as

$$\mathbf{F}_2 = \mathbf{f}_u |\nabla k|.$$

240 This choice of constraint enables to bring some structure to the parameter
241 field in a simple way. It can be noticed that this pre-factor is consistent
242 in terms of physical dimension with the divergence of the Reynolds stress
243 tensor. Given these two forms, two corrective models are then investigated.

244 *Parametrising the turbulence closure.* In contrast to a direct forcing on the
245 mean deformation field, corrections of the mean flow can still be embed-
246 ded under the Boussinesq hypothesis. Parameters are then included in the

247 turbulence model equations rather than at the level of the momentum equa-
 248 tions, and their effects on the mean flow are restricted to a purely diffusive
 249 mechanism. Under the realizable $k - \epsilon$ model framework, two possible cor-
 250 rective models can be designed: on the transport equation of kinetic energy
 251 k or on the equation of the dissipation rate ϵ .

252 In this work, only the correction of the transport of ϵ is considered since
 253 it is the equation where the closure terms are present. This choice keeps as
 254 much as possible the physical structure imposed by the RANS modelling.

255 As for its form, it can be assumed either that F_ϵ is an additive term
 256 without any particular structure as with \mathbf{F}_1 , or that it is an explicit function
 257 of ϵ . Consistently with [38], authors propose to pre-multiply the forcing term
 258 by ϵ in order to reject unphysical corrections at locations where turbulence
 259 is weak.

260 The following simple definition is considered

$$F_\epsilon = -f_\epsilon \epsilon,$$

261 in order to improve the robustness of the DA procedure.

262 3.4. Descent direction

263 The minimization is performed by a gradient-based algorithm which
 264 requires the evaluation of the objective functional gradient w.r.t the control
 265 variables α . To that end, the adjoint formulation [24, 49] is considered.
 266 In fact, the problem (1) is equivalent to the problem of determining the
 267 optimal state \mathbf{X} and the set of parameters α in addition to an adjoint state
 268 \mathbf{X}^* of a Lagrangian functional $\mathcal{L}(\mathbf{X}, \mathbf{X}^*, \alpha)$ [50]. It is defined by augmenting
 269 the functional \mathcal{J} with the constraint \mathbf{M} weighted by the adjoint state:

$$\mathcal{L}(\mathbf{X}, \mathbf{X}^*, \alpha) = \mathcal{J}(\mathbf{X}, \alpha) + \int_{\Omega} (\mathbf{X}^*)^T \mathbf{M}(\mathbf{X}, \alpha) \, d\Omega. \quad (5)$$

270 Then, by considering an infinitesimal perturbation of its arguments, set-
 271 ting the first variation of \mathcal{L} equal to zero leads to an optimality system,
 272 which provides the optimal solution.

273 In [38], a differentiation consistent both with the realizable $k - \epsilon$ trans-
 274 port equations and with the near-wall boundary layer law has been per-
 275 formed. This has resulted in the definition of a continuous adjoint RANS
 276 model, together with consistent associated boundary conditions of the RANS
 277 tangent linear operator.

278 Moreover, a gradient projection onto the Sobolev space [51] is also con-
 279 sidered for descent direction as an alternative regularization solution to
 280 penalization. As in the work of [38], the descent direction with Sobolev
 281 gradient is determined by solving the following equation

$$\frac{\partial \mathcal{L}^{H_1}}{\partial \alpha} = \left(\frac{1}{1 + l_{sob}^2} (\mathbf{I} - l_{sob}^2 \Delta) \right)^{-1} \frac{\partial \mathcal{L}}{\partial \alpha}, \quad (6)$$

282 in which the characteristic length scale l_{sob} , i.e. the filtering size, is chosen to
 283 smooth non-physical small scales and Δ stands for the Laplacian operator,
 284 while \mathbf{I} stands for identity. Note that, unlike with the penalization approach
 285 which requires an estimate of a non-dimensional confidence factor ζ with no
 286 direct physical significance, the free parameter l_{sob} has the dimensions of a
 287 length. This parameter can thus been chosen *a priori* based on a fraction
 288 of a relevant characteristic scales of the domain, such as the building width.

289 It is worth noting that this Sobolev gradient step can be presented as a
 290 standalone regularization technique without the addition of any penalization
 291 term on the control parameter. In this work, both techniques are considered
 292 individually. For conciseness, it is chosen to discuss their impact on the
 293 performances of the data-model coupling procedure when considering the
 294 additive forcing \mathbf{F}_1 .

295 4. Computational settings

296 Complying with the common standard [52], and consistently with [38],
 297 numerical computations are dimensioned with a full scale building.

298 4.1. Inflow wind profile: a neutral ABL

299 The atmospheric flow is modeled as a horizontally-homogeneous turbu-
 300 lent boundary layer (HHTBL) [53, 54]. This consists in considering constant
 301 properties in the streamwise and spanwise directions. Thus, only variations
 302 along the vertical axis are considered. To enforce the inlet wind flow, profiles
 303 for U , k and ϵ are defined as

$$U_{in} = \frac{u_\tau^{ABL} \ln(z + z_0)}{\kappa z_0}, \quad k_{in} = \frac{(u_\tau^{ABL})^2}{\sqrt{C_\mu}} \quad \text{and} \quad \epsilon_{in} = \frac{(u_\tau^{ABL})^3}{\kappa(z + z_0)}, \quad (7)$$

304 where $C_\mu = 0.09$ is chosen as for a standard $k - \epsilon$ model and u_τ^{ABL} is the
 305 friction velocity associated with the constant shear stress

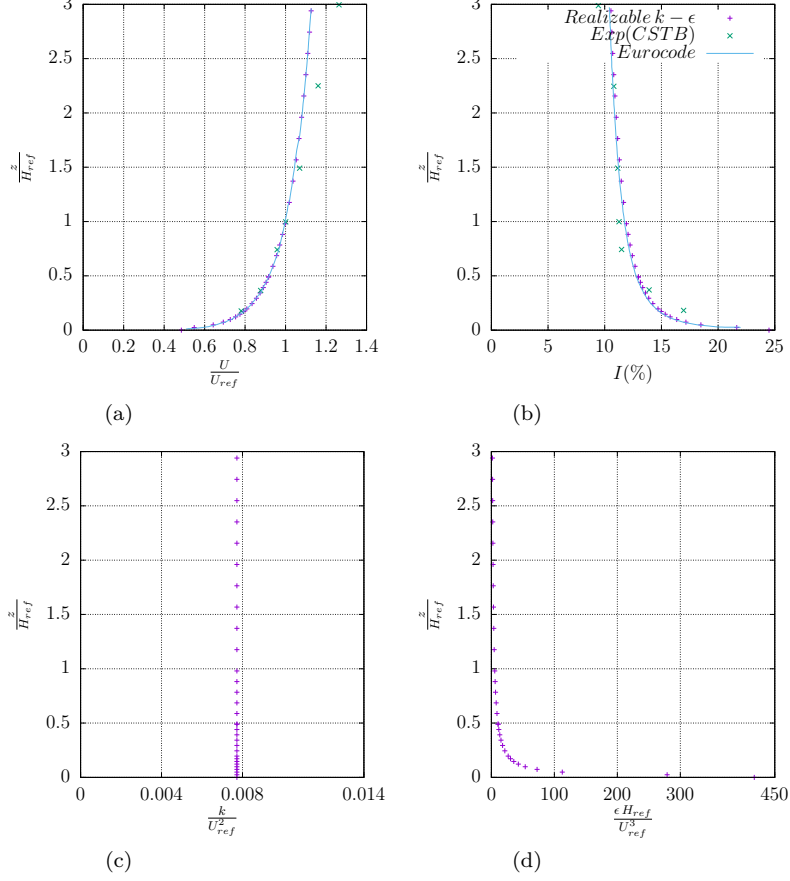


Figure 2: Profiles of the neutral atmospheric boundary layer: (a), mean wind velocity; (b), turbulent intensity $I = \frac{\sqrt{k}}{U_{ref}}$; (c), turbulent kinetic energy and (d), turbulence dissipation rate.

$$u_{\tau}^{ABL} = \frac{\kappa U_{ref}}{\ln\left(\frac{H_{ref} + z_0}{z_0}\right)}. \quad (8)$$

306 The roughness height z_0 is set to 0.02, which was chosen as an interme-
 307 diate between class I and class II roughness [52]. The inflow velocity profiles
 308 are shown in figure 2.

309 4.2. Computational domain

310 Based on recommendation by [16], in this work, the dimension of com-
 311 putational domain is fixed as $18H \times 12H \times 6H$ (length \times width \times height).
 312 This sufficiently large domain helps to avoid the influence of the domain

313 boundaries on the flow near the building and the wall-pressure. Meanwhile,
314 the upstream and downstream distances were set as $\sim 6H$ and $\sim 12H$,
315 respectively. The blockage ratio is 0.28 % less than the threshold of 3%
316 [16].

317 Hexagonal structured grid was adopted to generate the background
318 empty fetch, after which local mesh refinement approach was employed to
319 densify the grid around the building model, as shown in figure 1b. The min-
320 imum distance of grid centroid to the ground was set to $0.006 \times H$ (\sim one
321 meter) while it reaches down to $0.0008H$ for the centroid of the cell adjacent
322 to the building walls. The whole domain corresponds to approximately 3.5
323 millions cells.

324 4.3. Numerical method

325 The open source library OpenFOAM (5th version of the OpenFOAM
326 foundation) [55] was used to implement the CFD and adjoint governing
327 equations. The library utilizes a second order finite volume discretiza-
328 tion approach and a fully implicit first order method for time integration.
329 The variables are defined at the centers of each control volume (CV). A
330 prediction-correction procedure is used for the pressure-velocity coupling
331 using the SIMPLE-type methods with Rhie and Chow [56] interpolation.
332 With regard to the discretization schemes, the second order upwind (or
333 linear-upwind) scheme [57] is used for the advection terms as it is shown
334 to be one of the most efficient and accurate scheme for Reynolds Averaged
335 Navier–Stokes (RANS) simulations on bluff body flows [58].

336 4.4. VDA settings

337 Regarding the minimization procedure, a steepest descent algorithm is
338 used with an adaptive step. A maximum step size is fixed for each of the
339 parameters based on a prior sensitivity validation test, while a minimum
340 pre-factor for the step size of 10^{-4} is considered as an optimization conver-
341 gence criteria for all parametrisations.

342 Regularisation of the force parameter \mathbf{F}_1 is proceeded separately either
343 by the penalisation or by the prescription of the descent direction with
344 Sobolev gradient. The penalty-free parameter ranges in $\zeta_i = 0.1, 0.25, 0.5$.
345 Concerning the filtering length l_{sob} , as suggested in previous works [38, 59],
346 a filtering length scale equivalent to 10% of the building width seems to give
347 a fair compromise to filter unphysical small scales.

348 For the other parametrisation cases, only the Sobolev gradient is con-
349 sidered, with the same filtering length scale.

350 In the further investigation of combined parametrisations, penalty and
351 Sobolev gradient will be employed together to obtain an efficient regulari-
352 sation and capture physical flow features.

353 5. Results

354 This section is dedicated to the comparison of the different choices of
355 control parameter and regularisation techniques introduced in our data as-
356 simulation problem. The impact of their individual contribution on the wall-
357 pressure estimation and the wake flow reconstruction will be first explored.
358 Among all calculations presented in this paper, the case of control parameter
359 f_ϵ with Sobolev gradient regularisation is common with the study [38]. In
360 a second step, an efficient flow reconstruction by combining the advantages
361 identified in the previous techniques is proposed.

362 5.1. Choice of control parameter and regularisation

363 5.1.1. Cost reduction and convergence rate

364 *Evaluation of the regularization.* Reduction of the (normalized) cost func-
365 tional in the case of the forcing \mathbf{F}_1 on the momentum equation is com-
366 pared in figure 3a between Sobolev gradient and the penalty constraint.
367 With Sobolev gradient, the objective function has reached its lowest value
368 ($\mathcal{J}/\mathcal{J}_0 \simeq 0.2$). It should be noted nevertheless that with a penalty pa-
369 rameter set to $\zeta = 0.1$, a very close level of reduction $\mathcal{J}/\mathcal{J}_0 \simeq 0.26$ has
370 been reached, but after approximatively 5 times more iterations ($n_{it} \sim 500$
371 against 100 with Sobolev gradient). The faster minimisation and the lower
372 objective demonstrate the Sobolev gradient ability to improve significantly
373 the gradient-based algorithm. This is consistent with the observation in [38]
374 using the alternative control parameter f_ϵ . This improvement is at the price
375 of a low additional cost corresponding to the resolution of a Helmholtz like
376 equation, yet, of the same order as an additional iteration of the prediction-
377 correction loop. The filtering length l_{sob} can be chosen *a priori*, by taking
378 10% of the diameter of the building as characteristic length scale. It seems
379 to constitute a solid baseline. Indeed, a higher fraction leads to an overly-
380 diffused parameter, while lower values did not provide enough regulariza-
381 tion.

382 Note however that close to the optimal solution, the penalty provides a
383 better numerical behaviour, showing less oscillations around the minimum.

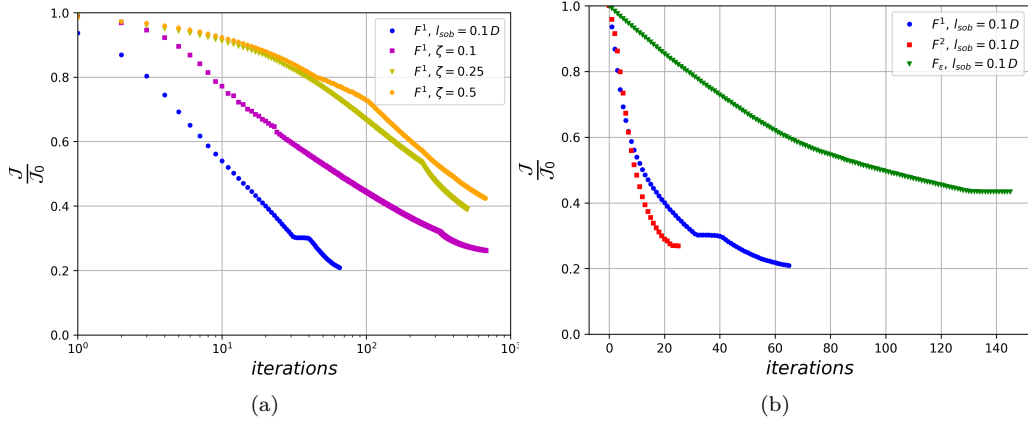


Figure 3: Cost function reduction with different parametrizations; (a) an added force F^1 with Sobolev gradient projection $l_{sob} = 0.1D$ against penalisation $\zeta = 0.1, 0.25, 0.5$, (b) comparison between all parameters with only Sobolev gradient projection.

384 *Evaluation of the parameter choice.* A comparison of the cost reduction with
 385 the different choices of parametrization is shown in figure 3b. It can be seen
 386 that using a structured force on the momentum equation \mathbf{F}_2 allows reaching
 387 an optimal objective at a level very close to the raw force \mathbf{F}_1 ($\mathcal{J}/\mathcal{J}_0 \simeq 0.27$),
 388 yet with a twice faster descent. This faster convergence suggests that adding
 389 a physical-based structure to the correction force seems to lead to a more
 390 efficient descent direction. Meanwhile, forcing with f_ϵ on the transport
 391 equation of ϵ leads to a lower cost reduction with more iterations. This is
 392 an expected result since it relies on a model that is further constrained, as
 393 highlighted in [38]. Recalling that the cost functional is representative of
 394 the building wall pressure. Due to potential overfitting effects, it is hard to
 395 conclude just in light of this result. Sections 5.1.3 and 5.1.4 explore velocity
 396 field reconstructions in the wake to obtain more prescriptive conclusions.

397 5.1.2. Wall pressure

398 Results of the pressure loads at and around measurement locations are
 399 compared with the experimental data [47] and the non-assimilated model
 400 in figure 4.

401 In the back facade, where $C_p < 0$, reconstructed wall-pressure with
 402 the raw force \mathbf{F}_1 shows perfect fitting to data, while the pre-multiplied
 403 force \mathbf{F}_2 and the forcing f_ϵ on the transport of ϵ lead to an intermediate
 404 estimation between model and data. Observing the windward and side
 405 facades and the roof top, it can be noticed that the forcing f_ϵ associated

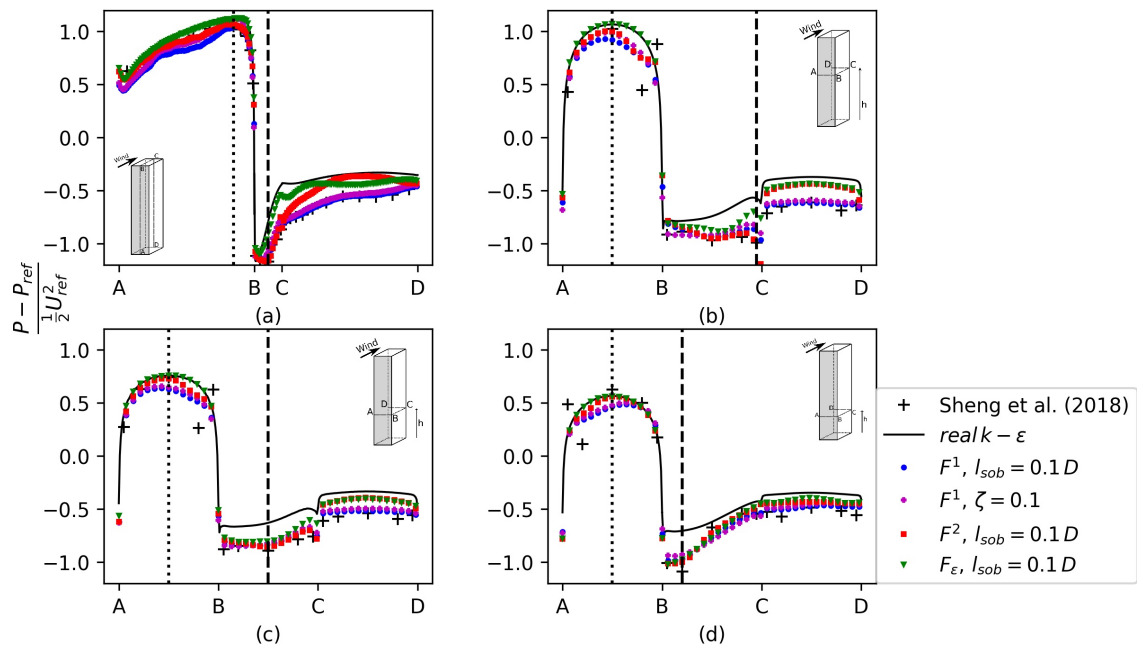


Figure 4: Pressure coefficient profiles along building facades with different parametrizations; (a) along the symmetry plane and along horizontal transverse plane at three heights, (b) $z/D = 3.33$, (c) $z/D = 0.9$, (d) $z/D = 0.63$.

406 with the most structured model leads to the closest results to the non-
 407 assimilated model, while the less structured model by a raw forcing \mathbf{F}_1 fits
 408 better the measurements. This is consistent with the results of section 5.1.1.
 409 A structured forcing on the momentum equation \mathbf{F}_2 leads to intermediate
 410 results.

411 If the objective of data assimilation is to perform wall pressure inter-
 412 polation between pressure taps enhanced by a RANS model, then the raw
 413 forcing on the momentum equation is well suited. The present results show
 414 that more structure forcings give more confidence in the model. In the next
 415 sections, a detailed comparison on the ability of these strategies is given in
 416 terms of velocity field reconstruction.

417 5.1.3. Wake centreline profiles

418 Results of the streamwise velocity on the wake centreline are here con-
 419 fronted to data from PIV experiments [47] and the uncorrected model in
 420 figure 5. It should be recalled that these data were not used in the as-
 421 similation problem. Hereafter, an up-wash (resp. down-wash) denotes the
 422 ascending (resp. descending) motions in the wake velocity field. In order to
 423 span both up-wash and down-wash motions, profiles are compared at four
 424 height levels ($z/D = 0.63, 1.26$ for up-wash and $z/D = 2.5, 3.33$ for down-
 425 wash). Moreover, at each height, a different recirculation length is iden-
 426 tified, by the intersection of the velocity profile with the axis $U/U_{ref} = 0$.
 427 As a first remark, all corrective models show some reduction at all heights.
 428 Yet, depending on the chosen parameter and the considered wake region,
 429 different reduction levels are achieved. With a parameter f_ϵ , data assimi-
 430 lation leads to the shortest recirculation among all parameters and regardless
 431 of the considered region, with a very good agreement with PIV data. For
 432 both momentum forcing strategies \mathbf{F}_1 and \mathbf{F}_2 , model abilities for retriev-
 433 ing the wake flow extension vary with the height and the forcing type. The
 434 most noticeable relative reductions are observed closer to the ground for the
 435 up-wash flow, with a very close prediction for both force shapes. However,
 436 in the down-wash flow region, a raw form leads to better wake reduction,
 437 while the structured forcing \mathbf{F}_2 leads to poor results.

438 At this stage, forcing on f_ϵ leads to good wake velocity field reconstruc-
 439 tion, but lower performances for pressure loads predictions and wall pressure
 440 interpolation. Meanwhile, a direct forcing on the momentum equation im-
 441 proves pressure prediction, but suspiciously by an unphysical mechanism,
 442 since it does not reduce the wake consistently with PIV measurements.

443 A second key aspect in the velocity profiles is the maximum reverse

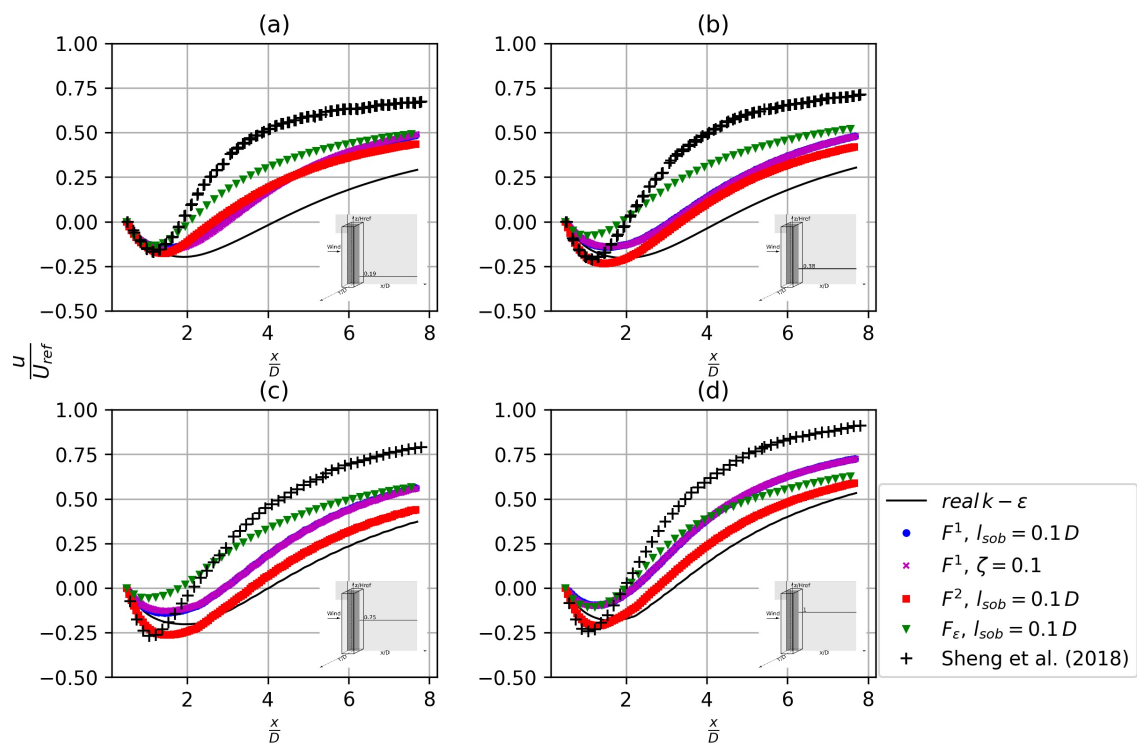


Figure 5: Streamwise velocity comparison along centreline at heights, (a) $z/D = 0.63$, (b) 1.25, (c) 2.5, (d) 3.33.

444 velocity, happening approximatively around $x/D = 1.5$ in the PIV mea-
 445 surements. Strong reverse flow is associated with intense depression and is
 446 thus indicative of the ability of the estimated wake to match the leeward
 447 pressure. The mismatch of the minimum velocity between PIV and model
 448 is especially strong for large z/D . Based on this criteria, forcing on f_ϵ and
 449 the direct raw forcing \mathbf{F}_1 shows bad performances, but surprisingly, the
 450 structured forcing on the momentum equation \mathbf{F}_2 leads to accurate max-
 451 imum reversed velocity in the wake. This is corroborated by the leeward
 452 pressure predictions in figure 4a), suggesting that the reasonable pressure
 453 predictions close to the high end (near point C) are obtained due to a good
 454 velocity prediction in the wake close to the building. It can be noted that
 455 in the case of raw forcing, regularisation effects are not visible in the wake
 456 centreline velocity profiles.

457 5.1.4. Reconstructing flow features

458 For a better insight into the reconstructed flow fields, figure 6 shows
 459 time-averaged sectional streamlines at symmetry plane. Note that sectional
 460 streamlines are computed by in-plane velocity components. In order to dis-
 461 cuss the flow topology, two specific points are to be observed. The first one
 462 is the saddle point observed at the frontier of the recirculation region, re-
 463 sulting from the interaction between the descending velocities (down-wash)
 464 and ascending velocities (up-wash) (for the uncorrected RANS model it is
 465 around $x/D \simeq 4, z/D \simeq 2$). The location of this point is strongly related to
 466 the recirculation lengths discussed in section 5.1.3. The second point is the
 467 focal point around ($x/D \simeq 1.5, z/D \simeq 4.5$) reminiscent of a large spanwise
 468 vortex structure, connecting the two symmetric recirculation vortices visi-
 469 ble in the horizontal plans in figures 7 and 8. This focal point is a sign of a
 470 local depression.

471 In the PIV symmetry plan, compared to the non-corrected models, the
 472 saddle point is located more upstream and slightly higher in z . Consistently
 473 with the results of section 5.1.3, the optimisations pull the saddle point
 474 upstream, but not sufficiently, and lower in z instead of being raised in
 475 the case of the structure-free forcing \mathbf{F}_1 . With the structured forcing \mathbf{F}_2 ,
 476 the z position of the saddle point is correct, but the recirculation length is
 477 too large. Forcing on the turbulence closure equation through f_ϵ leads to
 478 a drastic reduction of the recirculation region, and an accurate prediction
 479 of the saddle point position. As pointed out in [38], this striking result is
 480 mitigated by the fact that this saddle point has been pulled slightly too far
 481 upstream. Horizontal cross sections in figures 7 and 8 complement the view

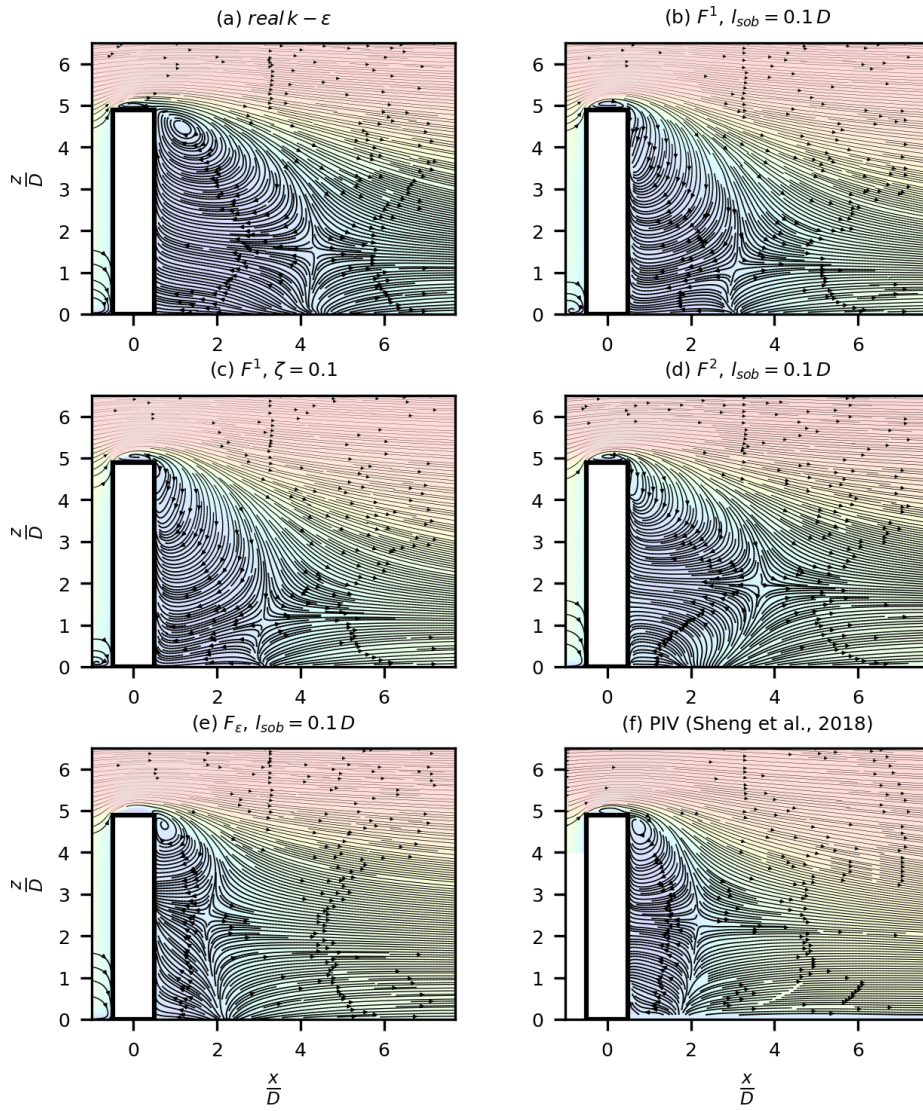


Figure 6: Flow topology (2D) comparison with the different proposed parametrization at symmetry plane.

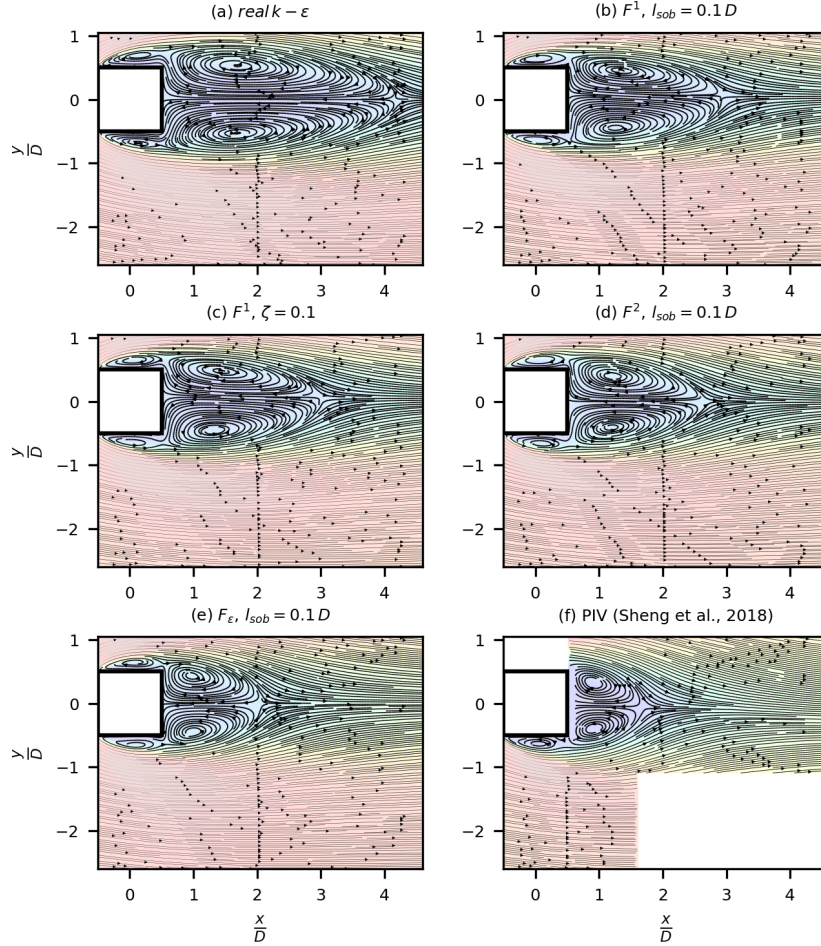


Figure 7: Flow topology (2D) comparison with the different proposed parametrization on horizontal plane at normalized height $z/D = 0.63$.

482 of the 3D flow structure.

483 Concerning the focal point in figure 6, complete disappearance is noted
 484 by the raw direct forcing \mathbf{F}_1 ; whereas it is moved upstream in the vicinity of
 485 the leeward facade in the case of structured force \mathbf{F}_2 . Yet, with the proposed
 486 closure parameter f_ϵ , this critical point is retrieved.

487 By taking these observations globally, it could be argued that the re-
 488 circulation region is globally reduced. This is, however, not achieved in an
 489 entirely satisfactory way with a raw force.

490 The results suggest that the pressure reduction in the leeward facade
 491 is performed in the optimisation by approaching the focal point very close

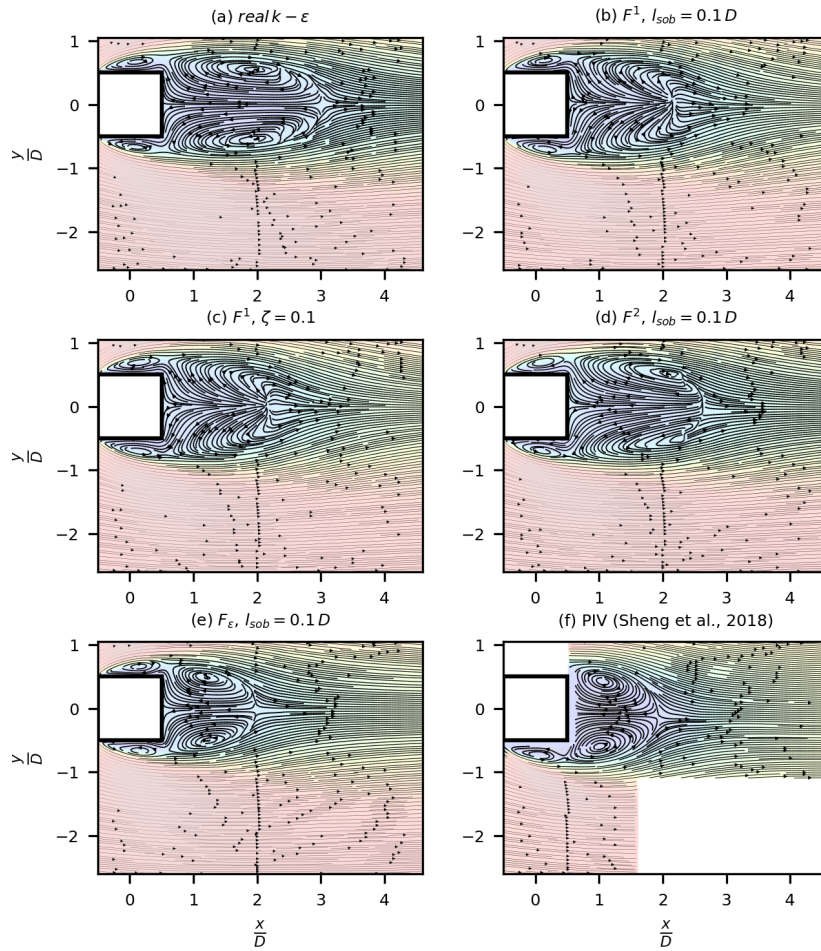


Figure 8: Flow topology (2D) comparison with the different proposed parametrization on horizontal plane at normalized height $z/D = 3.3$.

492 to the wall instead of significantly reducing the overall recirculation region.
493 This was not the case with f_ϵ as a control parameter, as the two-dimensional
494 vortices at both elevations ($z/D = 0.63, 3.33$) are still captured. Note
495 nonetheless that as one span downward, far enough from the high-end, such
496 that descending motions are negligible (say at $z/D = 0.63$), all models tend
497 to preserve the physical features (see figure 7).

498 Clearly, each parametrization has its pro and cons when applied indi-
499 vidually. Direct forcing, either structured or not, provides a superior ability
500 for wall-pressure interpolation, while embedding parameters in the turbu-
501 lence closure equation does preserve better the physical features of the wake
502 velocity field. To take advantage of both strategies, it is proposed next to
503 investigate the coupling of these two kinds of corrections. The choice of the
504 control parameter shape plays an important role here. Hence, performing
505 an efficient hybridisation is far from being an easy task as it requires proper
506 scaling between the two corrections.

507 *5.2. Exploiting complementary effects for reconstruction*

508 *5.2.1. Control parameters*

509 In order to refine flow reconstructions, this section considers simulta-
510 neously two kinds of control parameters; one forcing vector field acting on
511 the momentum equations and a scalar forcing field acting on the transport
512 equation of ϵ . In order to control better the rigidity of the model, a struc-
513 tured form of the forcing on the momentum equation is chosen. The present
514 choice is motivated based on the numerical tests performed in the previous
515 sections to act on two different physical mechanisms.

516 More precisely, the choice of the control parameter is motivated based
517 on the following observations. It has been shown in section 5.1 that forcing
518 directly on the momentum equation tends to lead to an overfitting of the
519 data. As a matter of fact, the wall pressure is well represented, but the flow
520 field is unphysical. A way to provide a better structure to this forcing is
521 to premultiply it by $|\nabla k|$. This still leads to a good reduction of the wall
522 pressure discrepancy, with performances in terms of the cost functional
523 decrease comparable to the direct forcing. Regarding the flow field, despite
524 a moderate reduction of the wake extension, the vertical position of the
525 saddle point is better recovered.

526 On the other hand, forcing on the transport of ϵ leads to impressive
527 reduction of the recirculation length. this can be interpreted by the fact that
528 it acts on the turbulent mixing, which is a key driver to simulate correctly
529 the wake shape. The disadvantage of this very structured model is that it

530 constraints severely the data assimilation process to reach in its exploration
 531 a sufficiently large domain of physical solution in the state space[38].

With the objective of performing the best flow reconstruction as possible, since they apparently act on two separate mechanisms, a combination of both strategies is investigated in the following. The model proposed in that aim reads as

$$\frac{\partial(\rho U_j U_i)}{\partial x_j} + \frac{\partial}{\partial x_i} \left(P + \frac{2}{3} \rho k \right) - \frac{\partial}{\partial x_j} \left[\mu_{eff} \left(\frac{\partial U_i}{\partial x_j} + \frac{\partial U_j}{\partial x_i} \right) \right] = -F_2 \quad (9a)$$

$$\frac{\partial U_i}{\partial x_i} = 0 \quad (9b)$$

$$M_k = 0 \quad (9c)$$

$$M_\epsilon = -f_\epsilon \epsilon \quad (9d)$$

532 where M_k and M_ϵ corresponds to the tubulent kinetic energy and tur-
 533 bulent dissipation evolutions of the base model.

534 5.2.2. Quality assessment for flow reconstructions

535 Validation metrics are defined here to evaluate the quality of the recon-
 536 struction. These metrics are proposed to compare the interpolation quality,
 537 i.e., the ability to reconstruct the wall pressure on the building based on
 538 sparse measurements, and the extrapolation/generalisation quality, i.e., the
 539 velocity field reconstruction. For the former purpose, the objective function
 540 \mathcal{J} is simply considered.

541 The wake reconstruction assessment is not straightforward. Consistently
 542 with the discussion of the velocity profiles in section 5.1.3, quantities repre-
 543 sentative respectively of the recirculation length and the maximum reverse
 544 flow velocity are defined. At a height z_j , \mathcal{M}_2^j measures the recirculation
 545 length relative error, defined as

$$\mathcal{M}_2^j = \left| \Delta L_x^j / \Delta L_x^{j,0} \right|, \quad (10)$$

546 with ΔL_x^j the error in recirculation length of the optimised model com-
 547 pared with PIV, and $\Delta L_x^{j,0}$ the error of recirculation length of the non-
 548 assimilated RANS model compared with PIV.

549 Similarly, the relative error of maximum reverse velocity at height z^j is
 550 defined by

$$\mathcal{M}_3^j = \left| \Delta U_{x_{\min}}^j / \Delta U_{x_{\min}}^{j,0} \right|, \quad (11)$$

	L_x^*	$U_{x_{\min}}^*$	$\mathcal{M}_2(\%)$	$\mathcal{M}_3(\%)$
Sheng et al. [47]	1.86, 2.13, 1.93	-0.170, -0.470, -0.421	-	-
realizable $k - \epsilon$	4.15, 4.01, 3.18	-0.197, -0.203, -0.181	100, 100, 100	100, 100, 100
$F_1, l_{sob} = 0.1 D$	2.92, 2.89, 2.16	-0.146, -0.138, -0.095	46.5, 40.3, 18.2	86.8, 124, 136
$F_2 = \nabla k f_u, l_{sob} = 0.1 D$	2.64, 3.56, 2.75	-0.177, -0.264, -0.211	33.9, 76.0, 65.6	26.7, 77.1, 87.5
$F_2, f_\epsilon, l_{sob} = 0.1 D$	2.43, 2.40, 2.33	-0.158, -0.120, -0.158	25.1, 14.5, 32.0	43.2, 131, 110
$F_2, f_\epsilon, l_{sob} = 0.1 D, (\zeta_{f_u}, \zeta_{f_\epsilon}) = (0.1, 15)$	2.29, 2.42, 2.36	-0.115, -0.105, -0.144	18.9, 15.3, 34.4	201, 137, 116
$F_2, f_\epsilon, l_{sob} = 0.1 D, (\zeta_{f_u}, \zeta_{f_\epsilon}) = (0.25, 15)$	2.18, 2.32, 2.30	-0.099, -0.091, -0.135	14.5, 10.0, 29.7	260, 142, 120
$F_2, f_\epsilon, l_{sob} = 0.1 D, (\zeta_{f_u}, \zeta_{f_\epsilon}) = (0.5, 15)$	2.22, 2.17, 2.25	-0.104, -0.080, -0.120	15.7, 2.20, 25.0	241, 147, 126
$f_\epsilon, l_{sob} = 0.1 D$	2.06, 1.77, 1.98	-0.135, -0.055, -0.106	8.69, 18.9, 3.94	129, 156, 131

Table 1: Normalized Recirculation length L_x^* and peak streamwise velocity U_x^* inside the recirculating flow at two height $z/D = (0.63, 2.5, 3.33)$ on the symmetry plane ($y/D = 0$) with different parametrization. Variables are normalized by D and U_{ref} , respectively.

551 where $\Delta U_{x_{\min}}^j$ stands for the error on the wake's peak velocity of the
552 optimised model compared with PIV, and $\Delta U_{x_{\min}}^{j,0}$ for the error on the max-
553 imum reverse velocity of the non-assimilated RANS model compared with
554 PIV.

555 As seen in section 5.1.3, it turns out that the two criteria \mathcal{M}_2 and \mathcal{M}_3
556 follow an opposite trend by varying the model rigidity, from an overfitted to
557 an over-constrained situation. A good estimation of the wake velocity field
558 consists of performing a trade-off between these quantities for all heights
559 z^j . It is then proposed to define the new quantity

$$A^2(\mathcal{M}_2, \mathcal{M}_3) = \frac{(1 - \frac{1}{n_z} \sum_j^{n_z} \mathcal{M}_2^j)}{\frac{1}{n_z} \sum_j^{n_z} \mathcal{M}_3^j} \quad (12)$$

560 where n_z denotes the number of considered heights. Here it should be
561 pointed out that a large value of $A^2(\mathcal{M}_2, \mathcal{M}_3)$ is the footprint of a good
562 estimation.

563 Yet, the choice of metric is not unique. The present choice has the
564 advantage of being more sensitive than a standard $L^2(\Omega)$ norm, by being
565 oriented toward a worst-case scenario in identifying maximum values. The
566 average over several peak values confers robustness to the metric.

567 The first two metrics are given in table 1, measured at three heights,
568 namely $z/D = 0.33, 2.5, 3.33$ in the symmetry plane.

569 Averaged metrics are collected in table 2. Tables summarize the current
570 (hybrid) parametrization results with different regularization levels: the
571 individual, direct forcing form, the structured force alone, and the corrected
572 closure on ϵ budget alone.

	$\varepsilon_{\mathcal{J}} = \mathcal{J}^{end} / \mathcal{J}^0 (\%)$	$A^1(\mathcal{M}_2) (\%)$	$A^1(\mathcal{M}_3) (\%)$	$A^2(\mathcal{M}_2, \mathcal{M}_3)$
Sheng et al. [47]	-	-	-	-
realizable $k - \epsilon$	100	100	100	-
$F_1, l_{sob} = 0.1 D$	20.9	35	116	0.56
$F_2 = \nabla k f_{u_i}, l_{sob} = 0.1 D$	26.9	58.5	<u>63.8</u>	0.65
$F_2, f_{\epsilon}, l_{sob} = 0.1 D$	23.7	23.9	94.6	<u>0.80</u>
$F_2, f_{\epsilon}, l_{sob} = 0.1 D, (\zeta_{f_{u_i}}, \zeta_{f_{\epsilon}}) = (0.1, 15)$	<u>20.3</u>	22.8	151	0.51
$F_2, f_{\epsilon}, l_{sob} = 0.1 D, (\zeta_{f_{u_i}}, \zeta_{f_{\epsilon}}) = (0.25, 15)$	25.2	18.1	174	0.47
$F_2, f_{\epsilon}, l_{sob} = 0.1 D, (\zeta_{f_{u_i}}, \zeta_{f_{\epsilon}}) = (0.5, 15)$	29	14.3	171	0.50
$f_{\epsilon}, l_{sob} = 0.1 D$	43.4	<u>10.5</u>	139	0.64

Table 2: Summarizing scores for reconstruction quality.

573 These quantitative comparisons are accompanied by graphs of the cost
574 function reduction, illustrated in figure 9, and wall-pressure distributions,
575 in figure 10. In the following, these tables and figures are discussed by
576 comparing the proposed criteria.

577 *Objective reduction assessment.* Among all tests performed, the best cost
578 functional reduction is obtained with the coupled scaling $(\zeta_{f_{u_i}}, \zeta_{f_{\epsilon}}) = (0.1, 15)$.
579 The reached performance is even better than when a direct raw forcing \mathbf{F}^1
580 without penalty (highly overfitted) was considered. In the following sec-
581 tions, the physical relevance of the flow structure in these cases is explored.

582 Employing penalty in conjunction with Sobolev gradient seems to im-
583 prove the cost functional reduction. Here, the effect of this is explored as
584 follows. Three penalization scaling factors of the momentum forcing were
585 considered: $\zeta_{f_{u_i}} = 0.1, 0.25, 0.5$, with a given penalization to ϵ fixed at
586 $\zeta_{f_{\epsilon}} = 15$. Fixing instead $\zeta_{f_{u_i}}$ and sweeping $\zeta_{f_{\epsilon}}$, leads to an opposite trend
587 since it is the ratio between them which drives the overall behaviour. As
588 expected, high values of $\zeta_{f_{u_i}}$ leads to large constraints for the optimisation,
589 while lower values does not efficiently suppress non-physical oscillations.
590 Moreover, it has been observed that $\zeta_{f_{u_i}}$ has a significantly higher impact
591 on the cost functional than $\zeta_{f_{\epsilon}}$. This is consistent with the fact that forc-
592 ing on the momentum equations allows modifying the wall-pressure easily.
593 Nonetheless, a high impact of $\zeta_{f_{\epsilon}}$ on the flow field should be expected, as f_{ϵ}
594 affects the bulk momentum diffusion.

595 *Wake predictions.* Examining the averaged flow metrics $A^1(\mathcal{M}_2), A^1(\mathcal{M}_3)$
596 reveals a reversed trend between them. The larger the reduction of the re-
597 circulation length, the worst the prediction of the peak streamwise velocity.
598 With no penalization considered, the only adjustment of the closure (by

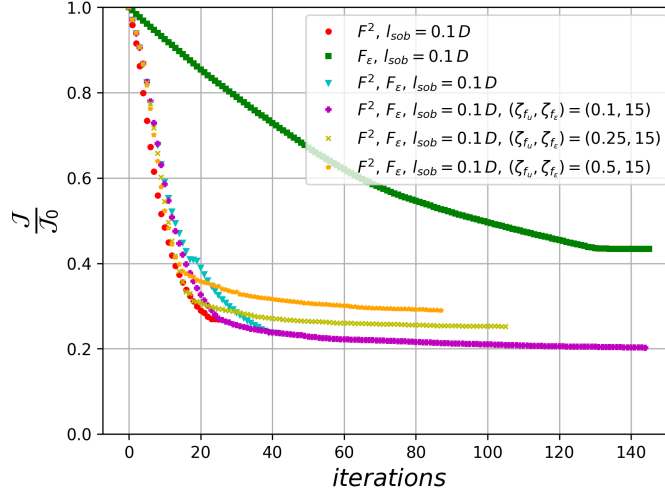


Figure 9: Cost function reduction under a correction of a structured force with a modified closure applied on ϵ budget for different penalization $(\zeta_{f_u}, \zeta_{f_\epsilon}) = ([0.1 \ 0.25 \ 0.5], 15)$. Comparison is made between raw-force (black circle), structured force (blue square), default closure, and modified closure made at the ϵ budget (yellow triangle).

599 f_ϵ) enables the lowest wake extension but leads to the slightest accurate
600 predictions, falling outside the base model error. On the other hand, the
601 only correction of the structured force leads to the least wake contraction
602 and the best error decrease.

603 To measure the trade-off between recirculation length and peak veloc-
604 ity, the quantity $A^2(\mathcal{M}_2, \mathcal{M}_3)$ (table 2) is introduced. From table 2, it
605 can be observed that the synchronous adjustment of the closure with the
606 force provides the better compromise ($A^2 = 0.8$), which is better achieved
607 with no penalization. It can also be seen that the direct forcing gives a
608 very low compromise ($A^2 = 0.56$) as compared with the most constrained
609 parametrization by only correcting f_ϵ ($A^2 = 0.64$). This supports the idea,
610 that this metric is only partially representative of the quality of reproduc-
611 tion of flow features.

612 By examining the flow topology, illustrated in figures 11 and 12, it can be
613 seen that correcting at the same time ($|\nabla k|f_u, f_\epsilon$) leads to an intermediate
614 solution between both individual corrections ($|\nabla k|f_u, 0$) and $(0, f_\epsilon)$.

615 It can be seen that recirculation region in the symmetry plane has sig-
616 nificantly reduced and a saddle point location in good agreement with PIV
617 data. However, it is still noted that the model excessively pulls the focal
618 point near the high end to the leeward facade, the mechanism employed

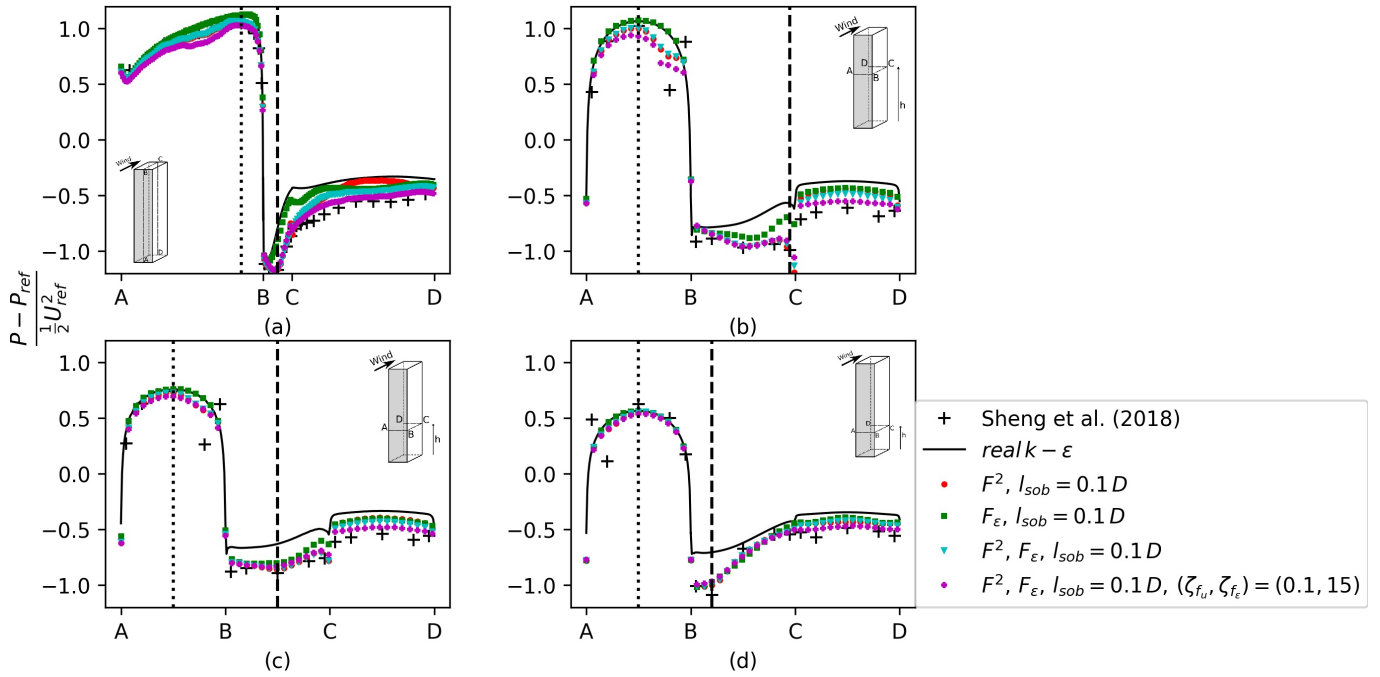


Figure 10: Pressure coefficient profiles along building facades under a correction of a structured force with a modified closure applied on ϵ budget for different penalization $(\zeta_{f_u}, \zeta_{f_\epsilon}) = ([0.10.250.5], 15)$. Comparison is made between raw-force (black circle), structured force (blue square), default closure, and modified closure made at the ϵ budget (yellow triangle).

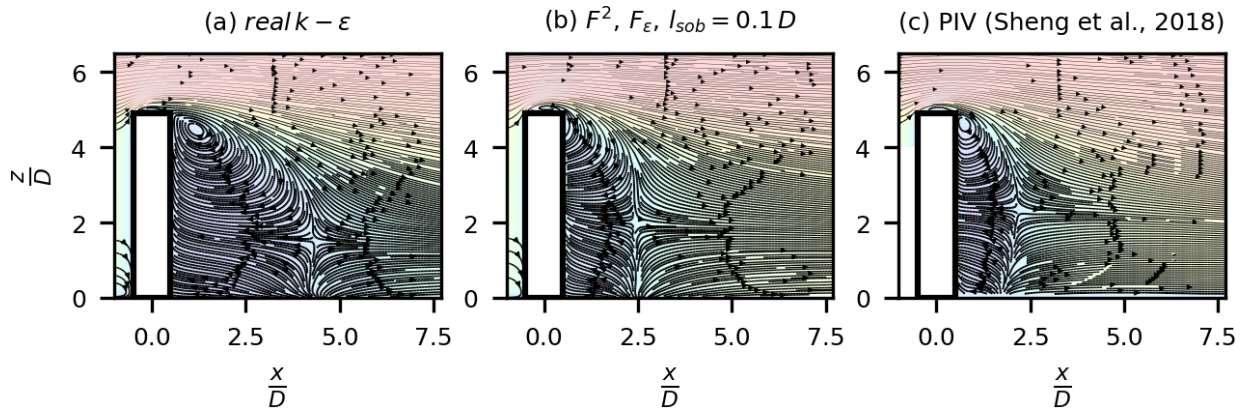


Figure 11: Flow topology (2D) with reconstruction under a correction of a structured force with a modified closure on symmetry plane.

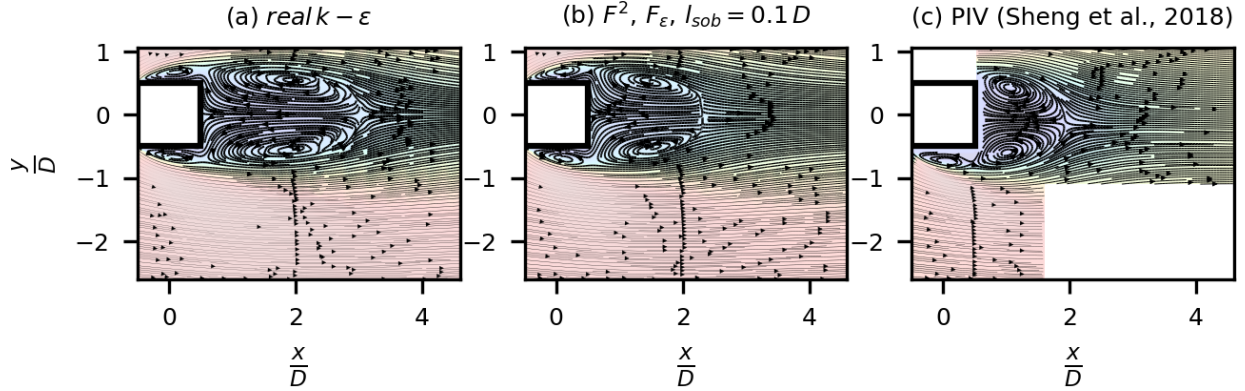


Figure 12: Flow topology (2D) with reconstruction under a correction of a structured force with a modified closure on horizontal plane at normalized height $z/D = 3.33$.

619 by the optimisation to fit the wall-pressure at the high end of the leeward
620 facade. Nonetheless, this remaining overfitting artifact is very limited in
621 space as the transverse structures are well retrieved. The reconstructed
622 flow still recovers the lateral vortex rolls, which extend from the ground
623 and meet at the high-end vortex on the symmetry plane, with the focal
624 points in the horizontal planes being well captured until height $z/D = 3.33$
625 with the downstream location of $x/D \simeq 1.5$. This location is intermediate
626 between the base RANS and the PIV ($x/D \simeq 1$) (see figure 12). Note that,
627 except with the correction of f_ϵ solely, both structured/raw form of forcing
628 with default closure does not capture them at all.

629 Therefore, by considering both the qualitative observations of the flow
630 features and the proposed wall/flow metrics, it can be summarized that
631 combination of a direct forcing on the momentum equation with simple
632 structuring form, along with a forcing on the transport equation of ϵ is a
633 promising strategy. It ensures overall a good quality to the reconstruction.
634 It is worth noting that although the quantitative flow metric A^2 did not
635 favors the penalization, examining the qualitative flow topology suggests
636 a better restitution of some physical features. It was observed by the re-
637 capturing of the high-end focal point with the couple of scaling $(\zeta_{f_{u_i}}, \zeta_{f_\epsilon}) =$
638 $(0.5, 15)$, which is otherwise absent (see figure 13). Therefore, providing
639 a penalization plays an important role in refining the flow features. Yet,
640 an adequate couple of scaling is required to provide a good compromise
641 between a well-interpolated wall pressure and the best retrieval of realistic
642 flow patterns.

643 Incorporating the forcing in the transport equation of turbulence dis-

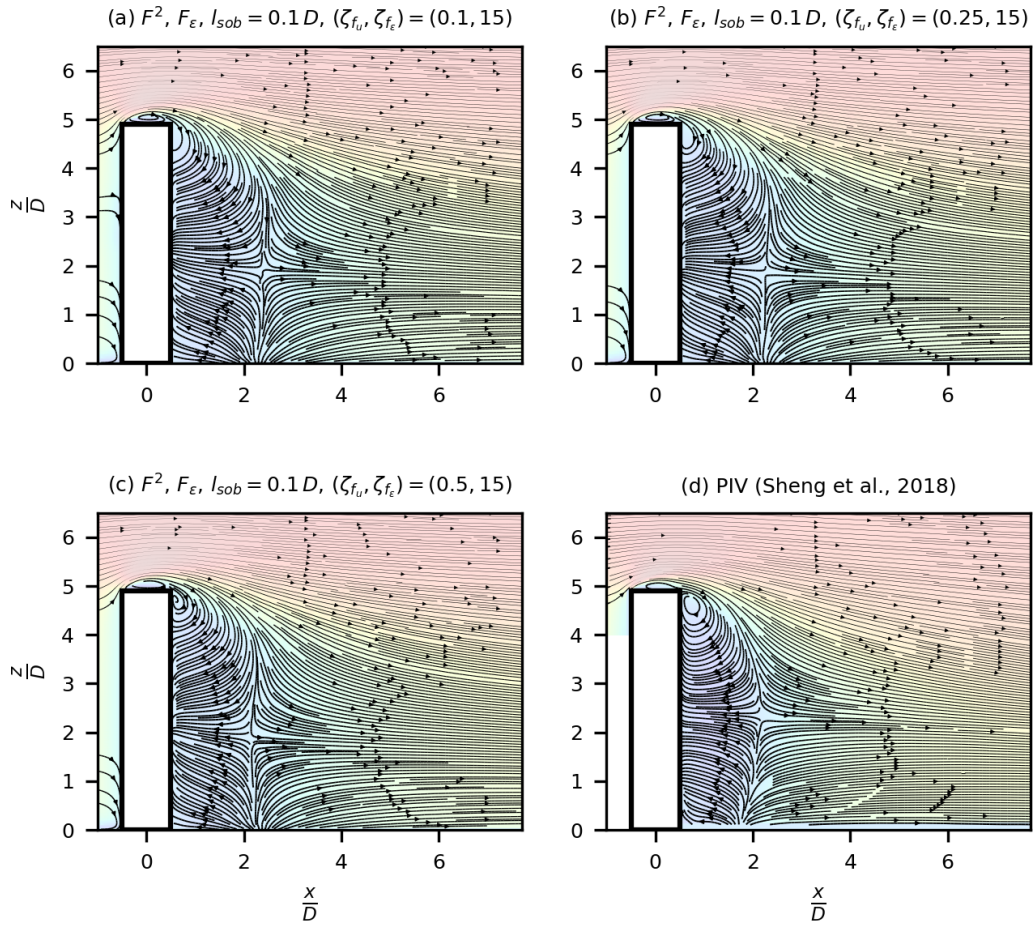


Figure 13: Flow topology (2D) on symmetry plane. Comparison with flow reconstruction, (a) under a correction of a structured force with a modified closure applied on ϵ budget with no penalization, (b) with penalization $(\zeta_{f_{u_i}}, \zeta_{f_\epsilon}) = (0.1, 15)$, (c) $(\zeta_{f_{u_i}}, \zeta_{f_\epsilon}) = (0.5, 15)$.

644 sipation rate reduces the overfitting. It suggests that the structure of the
645 RANS model is relevant and that the corrections to be added lye where the
646 closure is performed. This principle is likely generalisable for other models:
647 the control parameters should correct the closure models which are by def-
648 inition not fully known. The second main observation is that a very good
649 improvement is reached relaxing the Boussinesq assumption by a forcing on
650 the momentum equation. This suggests that in wake flows, the effect of
651 large scale structures and/or strong inhomogeneities and anisotropy (as in
652 shear layers) have a significant effect on the mean flow. Having accurate
653 results through a forcing on the momentum equation is a hard task since
654 an overfitting issue is faced. It is achieved thanks to the hybrid approach
655 that provides a forcing on both equations.

656 6. Conclusion

657 The present study aimed to investigate variational data assimilation
658 (DA) methodologies devised in previous work [38] to reconstruct 3D wind
659 flows around structures and provide guidelines toward an efficient recon-
660 struction. In this framework, the Reynolds Averaged Navier–Stokes equa-
661 tions (RANS) constitute the base mathematical model to describes the mean
662 wind flow. In particular, the case on which this study focuses on was ded-
663 icated to the analysis of a high-rise building with a square section and an
664 aspect ratio $H/D \sim 5$. For its improved capability to account for the energy
665 transfer with strong strain rates, the realizable revision developed by Shih
666 et al. [48] was also chosen as a reference turbulence closure. The inflow wind
667 profile models the lower part of the atmospheric boundary layer under the
668 assumption of horizontal homogeneity. The data considered for the assim-
669 ilation were the averaged wall-pressure measured on a scaled model of the
670 building in a wind tunnel experiment by Sheng et al. [47] at CSTB (Nantes,
671 France).

672 Several important findings arising from this study can be highlighted:

- 673 • In 3D wake flows, despite the fact than RANS models systemically
674 overpredict the recirculation length, wall-pressure information is a
675 meaningful enough piece of information to recover accurately exper-
676 imental wake extension;
- 677 • In weak constraint VDA, a control parameter on the transport equa-
678 tion within which the closure is performed avoids overfitting. Over-

679 fitting can be acceptable for wall-pressure interpolation, but reveals
680 catastrophic for wake flow reconstructions;

- 681 • A “hybrid” control parameter on the transport of ϵ and on the mo-
682 mentum equation leads to very accurate results due to a relaxation of
683 the Boussinesq assumption;
- 684 • Sobolev gradient descent direction leads to efficient regularisation and
685 to a fast convergence.

686 The present study constitutes a first step towards applying DA proce-
687 dure to real-world applications in structural wind engineering, where veloc-
688 ity field measurements of the whole 3D domain are not accessible. Note
689 that in this work, the quality of the data-assimilated flow field is quantified
690 by validation PIV data plans (but only wall-pressure measurements were
691 used for estimation). With the guidelines provided in this study, we can
692 imagine validations with more sparse and less costly measurements (sonic
693 anemometers) for estimations in operational conditions.

694 The reconstruction strategy employed in the present paper considered
695 a distributed additive forcing control parameter, acting on the momentum
696 equation and/or the transport equation of turbulent dissipations, where the
697 closure is performed.

698 In the first step, to recover the mean flow from the pressure measure-
699 ments, an unknown spatially distributed forcing was added to the momen-
700 tum equation in order to infer corrections to the Reynolds induced force.
701 Without a priori knowledge of its nature, an initial raw form was consid-
702 ered but led to unphysical oscillations. To avoid that, two regularization
703 approaches were investigated; the first one proceeded by penalizing the gra-
704 dient of the control parameter while the second was instead conducted by
705 Sobolev gradient [51, 59]. Regarding the effects of regularisation, cost re-
706 duction results with the Sobolev gradient yielded a much faster convergence,
707 lower discrepancy levels, and an excellent agreement with the wall-pressure
708 experiments in most building’s wall regions. An insufficient reduction of
709 the recirculation region, associated with non-physical features, has been ob-
710 served regarding flow reconstruction ability. It has raised the point about
711 the lack of structuration in the forcing.

712 In order to remedy this situation, authors proceeded by refining the
713 shape of the force with the aim to ensure some consistency with the forc-
714 ing directly related to the Reynolds stresses. To that purpose, a pre-
715 multiplication by the gradient of the kinetic energy favours corrections

716 where Reynolds stresses are likely active. In terms of objective, globally,
717 the discrepancy with wall-pressure experiments has been reduced signifi-
718 cantly and in a faster way, allowing us to reach a state very close to the
719 one achieved with raw forcing. Moreover, a better retrieval of the wake
720 features was noticed, particularly close to the ground reattachment point.
721 Unfortunately, it still leads to an insufficient reduction of the wake.

722 Alternatively, correction on the transport equation of ϵ was also con-
723 sidered. The modified closure produced a drastic improvement of the wake
724 extension, associated with a moderate performance of wall-pressure recon-
725 struction. This behaviour is well understood because acting near the turbu-
726 lence closure enables the maintenance of the model structure and avoiding
727 overfitting the wall pressure measurements. However, as the flow adjust-
728 ment comes only from diffusive effects, it suggests some room for improve-
729 ment with other forms of the (relaxing for instance the Boussinesq eddy
730 viscosity assumption) distributed parameters to obtain accurate flow esti-
731 mations.

732 With these results in mind, an intermediate solution was proposed.
733 While maintaining the Boussinesq assumption and correcting the turbu-
734 lence closure equation, an addition of a direct correction of the deformation
735 with a premultiplication factor is considered. To go toward an efficient
736 hybridization, control parameter forms have played a significant role here.
737 The reconstruction results were then discussed, and the quality of the recon-
738 struction was evaluated qualitatively and by the definition of some wall/flow
739 validations metrics. Both the qualitative and quantitative observations have
740 shown that the combination of a direct forcing with a simple structuring
741 form and local closure adjustment is a promising strategy as it ensures over-
742 all a good quality to the reconstruction.

743 It is interesting here to point out the great improvement in the predic-
744 tion of the tearing pressures, often the most important information needed
745 for dimensioning, goes with the improvement in the prediction of the wake.
746 Moreover, the conjunction of descent direction in H^1 and gradient penal-
747 ization in L^2 allows us to refine the quality of the flow estimation. Besides
748 the quality benefits on the final flow field, it was noticed that a robust DA
749 procedure could be ensured with the addition of penalty.

750 This allows to consider this kind of parametrization as a potential can-
751 didate for an efficient complex flow reconstruction given the limited amount
752 of data in hand. More so, with regards to the chosen parameters *forms*, the
753 authors are confident that this is quite generalizable as Boussinesq assup-

754 tion represents one fundamental bottleneck of the RANS modelling. It is
755 believed that this may represents an advancement over the state of the art
756 on flow reconstruction, and it constitutes an additional step toward more
757 challenges in wind engineering such as flow reconstructions around complex
758 buildings or within urban cities.

759 **Appendix A. Closure parameters in the realizable $k - \epsilon$ RANS** 760 **equations**

761 In this appendix, closure coefficients of the realizable $k - \epsilon$ RANS equa-
762 tions are detailed. First, σ_k (resp. σ_ϵ) is a closure constant, that allows the
763 turbulent mixing to have a different intensity in the momentum equations
764 than in the transport equation of kinetic energy k (resp. dissipation rate
765 ϵ). Besides, in the transport equation of ϵ ,

$$C_1 = \max\left(0.43, \frac{\eta}{(5 + \eta)}\right) \quad (\text{A.1})$$

766 with

$$\eta = Sk/\epsilon \quad (\text{A.2})$$

767 is the normalised strain rate. The constant C_2 is a closure coefficients.

768 Recall that the particularity of the realizable revision by Shih et al. [48] is
769 that the coefficient C_μ is a non uniform coefficient that depends on the mean
770 strain-rate and ensures the realizability conditions, i.e. Schwartz inequality
771 and the non-negativity of the diagonal Reynolds stress. It is defined by

$$C_\mu = \frac{1}{A_0 + A_s U_s \frac{k}{\epsilon}}, \quad (\text{A.3})$$

with

$$U_s = \sqrt{S_{ij}S_{ij} + \Omega_{ij}\Omega_{ij}} \quad (\text{A.4a})$$

$$S_{ij} = \frac{1}{2} \left(\frac{\partial U_i}{\partial x_j} + \frac{\partial U_j}{\partial x_i} \right) \quad (\text{A.4b})$$

$$\Omega_{ij} = \frac{1}{2} \left(\frac{\partial U_i}{\partial x_j} - \frac{\partial U_j}{\partial x_i} \right) \quad (\text{A.4c})$$

and

$$A_s = \sqrt{6} \cos(\phi), \quad \phi = \frac{1}{3} \arccos(\sqrt{6}W) \quad (\text{A.5a})$$

$$W = \frac{S_{ij}S_{jk}S_{ki}}{S}, \quad S = \sqrt{2S_{ij}S_{ij}}, \quad (\text{A.5b})$$

772 where S_{ij} and Ω_{ij} are, respectively, the mean strain (with its magnitude S)
773 and rotation rates. The parameter A_0 is a tuning coefficient.

774 References

- 775 [1] S. Murakami, A. Mochida, Y. Hayashi, S. Sakamoto, Numerical study on velocity-
776 pressure field and wind forces for bluff bodies by $k - \epsilon$, ASM and LES, *Journal of*
777 *Wind Engineering and Industrial Aerodynamics* 44 (1992) 2841–2852.
- 778 [2] P. A. Irwin, Bluff body aerodynamics in wind engineering, *Journal of Wind Engi-*
779 *neering and Industrial Aerodynamics* 96 (2008) 701–712.
- 780 [3] L. Cochran, R. Derickson, A physical modeler’s view of computational wind en-
781 gineering, *Journal of Wind Engineering and Industrial Aerodynamics* 99 (2011)
782 139–153.
- 783 [4] D. Surry, Wind loads on low-rise buildings: Past, present and future, *Wind Engi-*
784 *neering into the 21st Century* (1999).
- 785 [5] P. A. Irwin, W. W. Kochanski, Measurement of structural wind loads using the high
786 frequency pressure integration method, in: *Restructuring: America and Beyond*,
787 ASCE, 1995, pp. 1631–1634.
- 788 [6] R. J. Adrian, Particle-imaging techniques for experimental fluid mechanics, *Annual*
789 *review of fluid mechanics* 23 (1991) 261–304.
- 790 [7] G. Elsinga, F. Scarano, B. Wieneke, B. W. van Oudheusden, Tomographic particle
791 image velocimetry, *Experiments in fluids* 41 (2006) 933–947.
- 792 [8] S. Murakami, A. Mochida, K. Hibi, Three-dimensional numerical simulation of air
793 flow around a cubic model by means of large eddy simulation, *Journal of Wind*
794 *Engineering and Industrial Aerodynamics* 25 (1987) 291–305.
- 795 [9] S. Murakami, Computational wind engineering, *Journal of Wind Engineering and*
796 *Industrial Aerodynamics* 36 (1990) 517–538.
- 797 [10] S. Murakami, Comparison of various turbulence models applied to a bluff body, in:
798 *Computational Wind Engineering* 1, 1993, pp. 21–36.
- 799 [11] W. Rodi, Comparison of LES and RANS calculations of the flow around bluff bodies,
800 *Journal of Wind Engineering and Industrial Aerodynamics* 69-71 (1997) 55–75.
- 801 [12] T. G. Thomas, J. J. R. Williams, Simulation of skewed turbulent flow past a surface
802 mounted cube, *J. Wind Eng. Ind. Aerodyn.* (1999) 14.
- 803 [13] K. Nozawa, T. Tamura, Large eddy simulation of the flow around a low-rise building
804 immersed in a rough-wall turbulent boundary layer, *Journal of Wind Engineering*
805 *and Industrial Aerodynamics* 90 (2002) 1151–1162.
- 806 [14] B. E. Launder, B. I. Sharma, Application of the energy-dissipation model of tur-
807 bulance to the calculation of flow near a spinning disc, *Letters in Heat and Mass*
808 *Transfer* 1 (1974) 131–137.
- 809 [15] R. I. Issa, Rise of total pressure in frictional flow, *AIAA journal* 33 (1995) 772–774.
- 810 [16] J. Franke, C. Hirsch, A. Jensen, H. Krüs, M. Schatzmann, P. Westbury, S. Miles,
811 J. Wisse, N. Wright, Recommendations on the use of CFD in predicting pedestrian
812 wind environment, in: *Cost action C*, volume 14, 2004.
- 813 [17] A. Sohankar, L. Davidson, C. Norberg, Large Eddy Simulation of Flow Past a
814 Square Cylinder: Comparison of Different Subgrid Scale Models, *Journal of Fluids*
815 *Engineering* 122 (2000) 39–47.

- 816 [18] A. Gosman, Developments in CFD for industrial and environmental applications
817 in wind engineering, *Journal of Wind Engineering and Industrial Aerodynamics* 81
818 (1999) 21–39.
- 819 [19] G. Tabor, M. Baba-Ahmadi, Inlet conditions for large eddy simulation: A review,
820 *Computers & Fluids* 39 (2010) 553–567.
- 821 [20] M. S. Thordal, J. C. Bennetsen, H. H. H. Koss, Review for practical application
822 of CFD for the determination of wind load on high-rise buildings, *Journal of Wind
823 Engineering and Industrial Aerodynamics* 186 (2019) 155–168.
- 824 [21] P. Bergthörsson, B. R. Döös, Numerical weather map analysis, *Tellus* 7 (1955)
825 329–340.
- 826 [22] V. Mons, J. C. Chassaing, T. Gomez, P. Sagaut, Reconstruction of unsteady viscous
827 flows using data assimilation schemes, *Journal of Computational Physics* 316 (2016)
828 255–280.
- 829 [23] M. Meldi, A. Poux, A reduced order model based on Kalman filtering for sequential
830 data assimilation of turbulent flows, *Journal of Computational Physics* 347 (2017)
831 207–234.
- 832 [24] F. X. Le Dimet, O. Talagrand, Variational algorithms for analysis and assimilation
833 of meteorological observations: theoretical aspects, *Tellus A: Dynamic Meteorology
834 and Oceanography* 38 (1986) 97–110.
- 835 [25] P. Courtier, O. Talagrand, Variational assimilation of meteorological observations
836 with the adjoint vorticity equation. ii: Numerical results, *Quarterly Journal of the
837 Royal Meteorological Society* 113 (1987) 1329–1347.
- 838 [26] A. Gronsksis, D. Heitz, E. Mémin, Inflow and initial conditions for direct numerical
839 simulation based on adjoint data assimilation, *Journal of Computational Physics*
840 242 (2013) 480–497.
- 841 [27] Y. Yang, C. Robinson, D. Heitz, E. Mémin, Enhanced ensemble-based 4DVar scheme
842 for data assimilation, *Computers & Fluids* 115 (2015) 201–210.
- 843 [28] V. Mons, J. Chassaing, T. Gomez, P. Sagaut, Is isotropic turbulence decay governed
844 by asymptotic behavior of large scales? An eddy-damped quasi-normal markovian-
845 based data assimilation study, *Physics of Fluids* 26 (2014) 115105.
- 846 [29] V. Mons, L. Margheri, J. C. Chassaing, P. Sagaut, Data assimilation-based recon-
847 struction of urban pollutant release characteristics, *Journal of Wind Engineering
848 and Industrial Aerodynamics* 169 (2017) 232–250.
- 849 [30] P. Chandramouli, E. Memin, D. Heitz, 4D large scale variational data assimilation
850 of a turbulent flow with a dynamics error model, *Journal of Computational Physics*
851 (2020) 109446.
- 852 [31] D. Etling, H. W. Detering, F. Theunert, On the simulation of wind-driven currents
853 in shallow water, *Archives for meteorology, geophysics, and bioclimatology, Series
854 A* 33 (1985) 355–363.
- 855 [32] P. G. Duynkerke, Application of the $E - \epsilon$ turbulence closure model to the neutral
856 and stable atmospheric boundary layer, *Journal of the Atmospheric Sciences* 45
857 (1988) 865–880.
- 858 [33] S. Tavoularis, U. Karnik, Further experiments on the evolution of turbulent stresses
859 and scales in uniformly sheared turbulence, *Journal of Fluid Mechanics* 204 (1989)
860 457–478.
- 861 [34] H. Kato, S. Obayashi, Data Assimilation for Turbulent Flows, in: 16th AIAA

- 862 Non-Deterministic Approaches Conference, National Harbor, Maryland, 2014.
- 863 [35] W. N. Edeling, P. Cinnella, R. P. Dwight, H. Bijl, Bayesian estimates of parameter
864 variability in the $k - \epsilon$ turbulence model, *Journal of Computational Physics* 258
865 (2014) 73–94.
- 866 [36] L. Margheri, M. Meldi, M. V. Salvetti, P. Sagaut, Epistemic uncertainties in rans
867 model free coefficients, *Computers & Fluids* 102 (2014) 315–335.
- 868 [37] M. Shirzadi, P. A. Mirzaei, M. Naghashzadegan, Improvement of k-epsilon turbu-
869 lence model for CFD simulation of atmospheric boundary layer around a high-rise
870 building using stochastic optimization and Monte-Carlo sampling technique, *Jour-
871 nal of Wind Engineering and Industrial Aerodynamics* 171 (2017) 366–379.
- 872 [38] M. Y. Ben Ali, G. Tissot, D. Heitz, S. Aguinaga, E. Mémin, An adjoint approach for
873 the analysis of RANS closure using pressure measurements on a high-rise building,
874 2020. URL: <https://hal.archives-ouvertes.fr/hal-03076369>.
- 875 [39] D. P. G. Foures, N. Dovetta, D. Sipp, P. J. Schmid, A data-assimilation method
876 for Reynolds-Averaged Navier-Stokes-driven mean flow reconstruction, *Journal of
877 Fluid Mechanics* 759 (2014) 404–431.
- 878 [40] S. Symon, N. Dovetta, B. J. McKeon, D. Sipp, P. J. Schmid, Data assimilation of
879 mean velocity from 2D PIV measurements of flow over an idealized airfoil, *Experi-
880 ments in Fluids* 58 (2017) 61.
- 881 [41] K. Duraisamy, Z. J. Zhang, A. P. Singh, New approaches in turbulence and transi-
882 tion modeling using data-driven techniques, in: 53rd AIAA Aerospace Sciences
883 Meeting, Kissimmee, Florida, 2015.
- 884 [42] E. J. Parish, K. Duraisamy, A paradigm for data-driven predictive modeling using
885 field inversion and machine learning, *Journal of Computational Physics* 305 (2016)
886 758–774.
- 887 [43] A. P. Singh, K. Duraisamy, Using field inversion to quantify functional errors in
888 turbulence closures, *Physics of Fluids* 28 (2016) 045110.
- 889 [44] L. Franceschini, O. Sipp, D. and Marquet, Mean-flow data assimilation based on
890 minimal correction of turbulence models: Application to turbulent high Reynolds
891 number backward-facing step, *Phys. Rev. Fluids* 5 (2020) 094603.
- 892 [45] P. Spalart, S. Allmaras, A one-equation turbulence model for aerodynamic flows,
893 in: 30th Aerospace Sciences Meeting and Exhibit, Reno,NV,U.S.A., 1992.
- 894 [46] M. A. Iglesias, K. J. H. Law, A. M. Stuart, Ensemble Kalman methods for inverse
895 problems, *Inverse Problems* 29 (2013) 045001.
- 896 [47] R. Sheng, L. Perret, I. Calmet, F. Demouge, J. Guilhot, Wind tunnel study of wind
897 effects on a high-rise building at a scale of 1: 300, *Journal of Wind Engineering and
898 Industrial Aerodynamics* 174 (2018) 391–403.
- 899 [48] T. H. Shih, W. W. Liou, A. Shabbir, Z. Yang, J. Zhu, A new $k - \epsilon$ eddy viscosity
900 model for high Reynolds number turbulent flows-model development and validation,
901 Document ID: 19950005029 (Acquired Dec 28, 1995) Accession (1995).
- 902 [49] J. L. Lions, Optimal control of systems governed by partial differential equations
903 problèmes aux limites (1971).
- 904 [50] M. D. Gunzburger, Perspectives in flow control and optimization, volume 5, 2003.
- 905 [51] B. Protas, T. R. Bewley, G. Hagen, A computational framework for the regular-
906 ization of adjoint analysis in multiscale PDE systems, *Journal of Computational
907 Physics* 195 (2004) 49–89.

- 908 [52] N. EN, 1-4: Eurocode 1: Actions sur les structures–partie 1-4: Actions générales–
909 actions du vent, 2005.
- 910 [53] P. J. Richards, R. P. Hoxey, Appropriate boundary conditions for computational
911 wind engineering models using the $k-\epsilon$ turbulence model, in: Computational Wind
912 Engineering, 1993, pp. 145–153.
- 913 [54] P. Richards, S. Norris, Appropriate boundary conditions for computational wind
914 engineering models revisited, Journal of Wind Engineering and Industrial Aerody-
915 namics 99 (2011) 257–266.
- 916 [55] H. G. Weller, G. Tabor, H. Jasak, C. Fureby, A tensorial approach to computational
917 continuum mechanics using object-oriented techniques, Computers in physics 12
918 (1998) 620–631.
- 919 [56] C. M. Rhie, W. L. Chow, Numerical study of the turbulent flow past an airfoil with
920 trailing edge separation, AIAA journal 21 (1983) 1525–1532.
- 921 [57] R. F. Warming, R. M. Beam, Upwind second-order difference schemes and applica-
922 tions in aerodynamic flows, AIAA Journal 14 (1976) 1241–1249.
- 923 [58] E. Robertson, V. Choudhury, S. Bhushan, D. Walters, Validation of OpenFOAM
924 numerical methods and turbulence models for incompressible bluff body flows, Com-
925 puters & Fluids 123 (2015) 122–145.
- 926 [59] G. Tissot, R. Billard, G. Gabard, Optimal cavity shape design for acoustic liners
927 using Helmholtz equation with visco-thermal losses, Journal of Computational
928 Physics 402 (2020) 109048.